

# Asteroseismic modeling of delta Scuti stars: The cases of 44 Tau and HD 187547

Janne Højmark Mønster, 201405523  
Aarhus University, Department of Physics and Astronomy

August 31, 2019



# 1 Acknowledgements

First and foremost, I would like to express my sincere gratitude to the people who have helped me through my research, making this thesis possible. A very special thanks my co-supervisor Victoria Antoci, who not only opened my eyes to the exciting field of asteroseismology, but made the project entirely possible. She has guided me to become a better researcher, and this thesis is a product of that. Also a big thanks to my main supervisor Günter Houdek who helped me during the enormous task of grasping the concepts behind numerical simulations and the theory of stellar structure and evolution.

I am also extremely grateful for the help provided by Earl Bellinger, without whom I would have probably still been stuck in a forloop. His knowledge in computer science has helped me on countless occasions to increase my coding skills.

This research would not have been carried out without the help of my office mates who have lend an ear to many frustrated hours of writing, coding and reattempting. Thanks to Simon Banerjee for always being ready to discuss problems, to Rasmus Lind Bjerre for putting a smile back onto my face when I was struggling and to Dorte Thrigle Plauborg who has been my rock to lean on throughout the entire process. Finally, I wish to thank all my friends and my family for the support and understanding I have received. A heartfelt thanks to my boyfriend Emil Christensen who always kept understanding, supporting and loving me.

# Contents

<b>1 Acknowledgements</b>	<b>3</b>
<b>Contents</b>	<b>4</b>
<b>2 Introduction</b>	<b>7</b>
<b>3 Stellar Structure and Evolution</b>	<b>9</b>
3.1 Energy transport by convection . . . . .	10
3.2 Stellar evolution through the HR-diagram . . . . .	13
<b>4 An introduction to asteroseismology</b>	<b>19</b>
4.1 Stellar pulsations . . . . .	19
4.1.1 Pressure and Gravity modes . . . . .	21
<b>5 The Delta Scuti stars</b>	<b>27</b>
5.1 The pulsation HR-diagram and the driving mechanisms . . . . .	27
5.2 Why Delta Sct stars? . . . . .	29
5.3 The delta Scuti stars 44 Tau and Superstar . . . . .	30
5.3.1 44 Tau . . . . .	30
5.3.2 HD 187547 . . . . .	32
<b>6 Computational tools</b>	<b>35</b>
6.1 MESA . . . . .	35
6.1.1 Stellar structure and evolution . . . . .	35
6.1.2 Output . . . . .	37
6.1.3 Convection treatment . . . . .	37
6.1.4 Element abundance mixtures . . . . .	39
6.1.5 Equation of state . . . . .	40
6.1.6 Opacity data . . . . .	41
6.2 GYRE . . . . .	41
6.2.1 Input and output options . . . . .	42
<b>7 Modeling 44 Tau and Superstar</b>	<b>45</b>
7.1 Choosing a grid . . . . .	45
7.2 Resolution and varcontrol . . . . .	49
7.3 chi2 testing . . . . .	51
7.3.1 Finding the best model . . . . .	51
7.3.2 44 Tau . . . . .	52
7.3.2.1 l=0 modes . . . . .	52
7.3.2.2 l=0,1,2 modes . . . . .	56
7.3.3 Results . . . . .	57
7.4 Superstar . . . . .	61
7.4.1 Results . . . . .	62

<i>CONTENTS</i>	5
<b>8 Discussion and future work</b>	<b>67</b>
8.1 Grid considerations . . . . .	67
8.2 Stringent statistics . . . . .	69
<b>9 Conclusions</b>	<b>71</b>
<b>Bibliography</b>	<b>73</b>



## 2 Introduction

The field of astronomy is one of the oldest sciences in the world, attempting to answer any question on the universe an the celestial bodies within it. Throughout the years it has developed into several theoretical and observational branches studying every corner of the universe from the nearest objects such as the moon an the Sun to the very edges of the universe that are so far away that the human brain cannot grasp the sheer size of it. Since the early studies to present day, astronomy has developed substantially, yet many questions remain still unanswered. What does the universe consist of? How old is the universe? Why are we able to exist here on Earth? Some of these may not be answered ever, yet curiosity drives humans to continue researching.

One of the major components in the universe is the stars. New stars are born from the "ashes" of dead stars and learning how they are formed, evolve and die is fundamental for understanding the environment they evolve in. Such studies are within the field of *Stellar Structure and Evolution*. Describing the different type of stars is an immense task in itself and dividing them into categories and understanding them requires us to understand the processes that leads to differences in their stellar structures. The problem with this is, however, that the insides of stars is unreachable from an observational point of view. We cannot simply look inside the stars, and for a long time penetrating the barriers of stellar layers seemed unobtainable.

Records on observations of pulsating stars goes back nearly 500 years. It was not until 1980's that we fully understood the potential of pulsations. At this point, the field of *asteroseismology* was introduced by Christensen-Dalsgaard (1984) as "The science of using stellar oscillations for the study of the properties of stars, including their internal structure and dynamics".

The closest (and therefore most studied) star is the Sun. Knowledge provided from the Sun can be projected to other types of stars, and *helioseismology* (asteroseismology of the Sun) has provided valuable research in the field of Stellar Structure and Evolution. However, helioseismology is not yet developed enough to reach the deepest layers of the Sun where the core resides. Therefore, we need to turn to other types of stars and exploit their pulsational advantages to reveal the secrets inside the stars.

Before computers were invented, every observation and calculation were done analytically, which was a very time consuming task. Full stellar evolution tracks could simply not be carried out. However, we are now at a time where stellar evolution can be calculated fully numerically and results compared to the expected parameters derived from observations. Stellar structure and evolution codes can further provide calculations of the pulsations in a star with a stellar pulsation code. This is crucial for stellar modeling as the pulsation frequencies acts as an additional constraint to the parameter space. This constrain can help identify the processes inside pulsating stars, and thereby obtain knowledge on the pulsation mechanism, structure, convection, and evolutionary stage.

In this work the method of asteroseismic modeling is applied to two different  $\delta$  Sct stars, 44 Tau and 187547 (From here on referred to as Superstar). 44 Tau

has already been modeled which to estimate the the evolutionary stage. By using a similar method in this work and comparing results, the procedure can be evaluated and adjusted to further be applied to Superstar. Asteroseismic modeling is particularly needed for this star since it represents some of the issues with the theory behind  $\delta$  Sct stars. The goal of the asteroseismic modeling in this work is ultimately to analyze how well theory matches observations and using the results to discuss the remaining issues in the field and optimize the methods for any future work. The work can be utilized on other types of stars, so a deeper understanding of stellar structure and evolution in general can be achieved. Hence, we get one step closer to understanding one of the most fundamental parts of the universe.

The work is structured as follows: Chap. 3 gives an introduction to Stellar structure and evolution related to this work. Relevant numerical results are presented to demonstrate key aspects of the field. Chap. 4 introduces the theory behind asteroseismology, and how it can be applied to various types of star, depending on the structure of the star. In Chap. 5 the  $\delta$  Sct stars described in more detail with the focus being on their importance from an asteroseismic and modeling point of view. Specifically, the asteroseismic and observational background of 44 Tau and Superstar are introduced. The tools used for modeling these star are presented in Chap. 6, where the Stellar Structure and Evolution code **MESA** and Stellar Pulsation code **GYRE** and their main numerical aspects are presented. Chap. 7 described the entire process of modeling the stars and the methods applied to compare to observations. Main results and proposed future work is then discussed in Sec. 8 and final conclusions are given in Chap. 9.

This work has made use of data from the European Space Agency (ESA) mission Gaia (<https://www.cosmos.esa.int/gaia>), processed by the Gaia Data Processing and Analysis Consortium (DPAC, <https://www.cosmos.esa.int/web/gaia/dpac/consortium>). Funding for the DPAC has been provided by national institutions, in particular the institutions participating in the Gaia Multilateral Agreement.

# 3 Stellar Structure and Evolution

The field of stellar structure and evolution is wide and it is possible to study numerous aspects of it. In this section, a brief introduction to the theory of stellar structure and evolution is given. This is based on mainly Christensen-Dalsgaard (2008b) and Kippenhahn et al. (1990).

It is difficult to paint a general picture of a "star". There are several types, depending on both observable properties such as magnitude and effective temperature, but also indirect properties such as structure and oscillation modes. Assumptions and simplifications are therefore necessary in order to give a comprehensible representation of a star. First, and foremost, a star is always assumed to be in *hydrostatic equilibrium*, meaning that physics on a macroscopic level adapts to the surroundings on a timescale much faster than the *free-fall time* (i.e. the time it takes until the interstellar cloud has contracted to a point). The star is also assumed to have none or little rotation such that it can be treated as spherically symmetric. Magnetic fields are likewise assumed to not be present in the star. These assumption are of course very crude, as we know that stars do indeed rotate and have magnetic fields. However, the assumptions provides us the possibility to give a rough estimate on the conditions in a star.

A star in hydrostatic equilibrium balances its own gravitation with the pressure from radiation. By looking at an infinitesimal mass element  $dm$  at a distance  $r$  from the center, one can derive

$$\frac{dP}{dr} = -\frac{GM(r)}{r^2}\rho \quad (3.1)$$

where  $G$  is the gravitational constant and  $P$  is the pressure. This equation states that the pressure obtained from gas and radiation must be equal to that of gravitation in order to maintain hydrostatic equilibrium. It can be rewritten in the alternative form

$$\frac{dM(r)}{dr} = 4\pi r^2\rho, \quad (3.2)$$

where  $M(r)$  is the mass of a spherical shell of radius  $r$ . Combining the two equations yields

$$-\frac{dP}{dM(r)} = \frac{G}{4\pi} \frac{M(r)}{r^4}. \quad (3.3)$$

From these equations it is possible to derive expressions for the minimum value of the central pressure  $P_c$ , the mean pressure  $\tilde{P}$  and temperature  $\tilde{T}$  for the case of a homogeneous star (i.e.). Here, no knowledge on the composition is required, only the mass distribution.

For a more thorough description of stellar structure, the properties of the matter needs to be assessed. Describing the thermodynamical properties in

detail is no simple task, but the fundamental assumption is that at any point in the star, the gas is assumed to be in *thermodynamic equilibrium*, which means that there are no net macroscopic flows. This approximation ensures that instead of considering detailed reactions between particles, the average properties of the gas can be described by local state variables. The relations between these specifies the *equation of state* (EOS) of the gas. It is also assumed that there is no change in the gas conditions over the distance of the mean-free-path of a particle located in the gas, or over the time between collisions. These assumptions are well applied in stellar interiors, but in order to describe conditions in the atmosphere, a more detailed description is needed.

Since temperatures in the interiors are high, most of the gas will be fully ionized, and thereby have no internal degrees of freedom. Interactions b (collisions) between particles can be neglected, hence the gas is an approximate *ideal gas* following the ideal-gas law

$$PV = Nk_B T, \quad (3.4)$$

where  $N$  is the number of particles in a gas with volume  $V$ , and  $k_B$  is Boltzmann's constant. From this, general relations between pressure and internal energy can be derived. Stellar structure and evolution solves both equations of hydrostatic equilibrium and the EOS of the star. The modules used in this project will be described in Chap. 6.

### 3.1 Energy transport by convection

When deriving the equations and variables for a star, it is usually assumed that the star can be treated as being spherically symmetric. In reality though, there will be fluctuations on small scales that has to be taken into account. The most considered of these instabilities or fluctuations is the *convection*. These can be treated as small perturbations.

Convection can be described as macroscopic mass elements or "bubbles" that transports energy in a star. Elements that are hotter than their surroundings rises upwards carrying excess thermal energy. The displacement of the element grows exponentially and when the velocity becomes too large, nonlinear effects causes the thermal energy to be released into the surroundings. Thus, convection contributes by transporting energy, and mixing the gas elements. This has large consequences for the stellar evolution as we shall see in Sec. 6.

Whether a region in a star is stable against convection depends on whether the perturbation is allowed to grow under certain conditions. Therefore, it is a matter of *convective instability*. Assuming that the mass elements does not exchange energy with the surroundings (during movement), and therefore moves adiabatically, it can be derived that

$$\nabla < \nabla_e + \frac{\phi}{\delta} \nabla_\mu, \quad (3.5)$$

where

$$\nabla \equiv \left( \frac{d \ln T}{d \ln P} \right)_s, \quad \nabla_e \equiv \left( \frac{d \ln T}{d \ln P} \right)_e, \quad \nabla_\mu \equiv \left( \frac{d \ln \mu}{d \ln P} \right)_s. \quad (3.6)$$

Here, the subscript  $e$  means that the derivative is in relation to the element, whereas  $s$  is the surrounding material. For the case where energy is transported by radiation or conduction only

$$\nabla_{rad} \equiv \left( \frac{d \ln T}{d \ln P} \right)_{rad}, \quad (3.7)$$

temperature variations is described with depth. In a layer where all energy transport is either radiation or conduction,  $\nabla = \nabla_{rad}$ . Also, assuming that the element moves adiabatically such that

$$\nabla_e = \nabla_{ad} \equiv \left( \frac{\partial \ln T}{\partial \ln P} \right)_s \quad (3.8)$$

and inserting in Eq. 3.5, one arrives at

$$\nabla_{rad} < \nabla_{ad} + \frac{\phi}{\delta} \nabla_\mu, \quad (3.9)$$

known as the *Ledoux criterion*. Under the assumptions mentioned earlier, this is the criteria for dynamical instability. It can be simplified further by assuming that the chemical composition is homogenous throughout the star such that  $\mu = 0$ . This yields the *Schwarzschild criterion* on the simple form:

$$\nabla_{rad} < \nabla_{ad}. \quad (3.10)$$

This assumption does not apply well to evolving stars where elements are not necessarily produced in the same layer (as heavier elements are produced below lighter). Instability to convection thus occurs when the left hand side becomes larger than the right hand side. The small perturbations will grow until the layers is filled with convection. This occurs if

- $L(r)/m(r)$ , (the energy generation rate per unit mass within radius  $r$ ) is large. In massive stars, this rate is an increasing function of temperature, thus increasing  $L/m$  towards the centre. Therefore these stars have convective cores.
- $\rho/T$  is large. Since  $\rho/T^3$  increases rapidly in the photosphere, this usually occurs in cooler stars.
- The opacity  $\kappa$  is large. Stars with low surface temperatures usually have higher  $\kappa$  in the outer layers.
- $\nabla_{ad}$  is small. This happens in hydrogen ionization zone, like  $\kappa$ , in outer layers of cool stars.

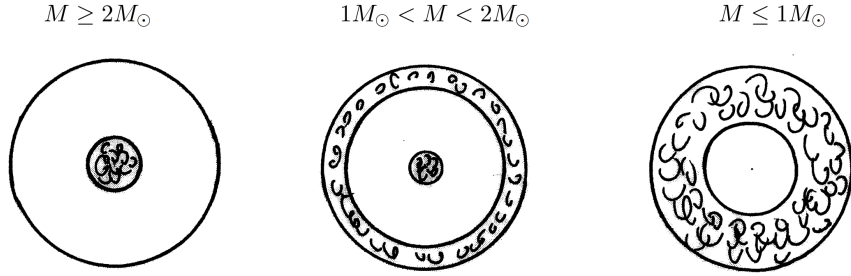


Figure 3.1: Estimated occurrence of convection zones in main-sequence stars with different masses. Stars with masses higher than  $2 M_{\odot}$  have fully convective cores and only a very thin convective shell. Less massive stars with masses below  $1 M_{\odot}$  have deep convective envelopes. The stars in between marks the transition between the two. They have convective cores and a thin convective outer layer.

To sum up, the first condition consequently allows for convection in the core of massive stars. The remaining conditions for outer layers of cooler stars. The different possibilities for the structures are illustrated on Fig. 3.1.

The stars in this project lies in the *intermediate mass* range which is usually stars of masses between  $1.5 M_{\odot}$  and  $2.2 M_{\odot}$ . They cover the transition from deep convective envelopes and convective cores. The motivation for using such stars will be discussed further in Sec. 5.2.

If the criteria leads to stability it follows that  $\nabla = \nabla_{rad}$  for the entire layer. The last possibility is that there one of Eq. 3.8 and Eq. 3.9 says stability whereas the other says instability. This is called the Twilight zone, see (Kippenhahn et al., 1990) for more details.

This prescription gives a very simplified picture of where convection is expected to occur within a star. However, in reality a local treatment is complicated since convective motion is not only dependent on local forces, but forces between layers as well (such as momentum and inertia). The border of a convective zone is thereby not well-defined and precise as elements accelerated from one layer might flow into another. This will be discussed further in Sec. 6.1.3. Convection flows in the laboratory is relatively well described by reasonable approximations. However, in stars convection is happening in much more violent conditions where compression of gas and turbulent motion depends on density, pressure and gravity of very high orders. Taking such effects into consideration is not simple by any means, but efforts have been made to implement convection by making full two- and three-dimensional hydro dynamical simulations. (Nordlund & Stein, 1990). These codes does not treat the convection as separate homogeneous bubbles, but as a fully coupled time-dependent system. Such codes give a much more detailed and realistic picture of convection for single models. However, since the computation time for the full convective solution of a model is much higher than a simplified version, calculating a full track is not yet feasible. Therefore, the most used method

is the *standard mixing length theory*, which is a time-independent assessment. This is not sufficient to describe full hydrodynamical convection, but allows approximations to give a simplified local treatment, where convection can be described as macroscopic mass elements transferring energy. The mean free path is described with the *mixing length*. There are several ways to implement this in stellar modeling which will be described in Sec. 6.1.3.

## 3.2 Numerical results for stellar evolution through the HR-diagram

This section describes the evolution of a star through numerically calculated stellar evolutionary tracks, mainly focusing on the main sequence (ms)) and immediate post-main sequence (pms) phases of intermediate mass stars

Stars are born from molecular clouds, collapsing under their own gravity. When the cloud reaches a the *Jeans Mass*, the *Jeans Criterion* is fulfilled, meaning that any perturbation will cause a free-fall collapse. This continues while the process happens isothermally until the free-fall time becomes similar to the timescale for thermal adjustment. The process then becomes adiabatic, stopping the rapid dynamical contraction and leaving behind a *protostar* in hydrostatic equilibrium. Due to their low internal temperature and high opacity, these stars are fully convective. Thereby they are born on the *Hayashi Track* where the contraction continues. This track is the beginning of the *pre-main sequence phase*. As the star contracts and descends on the Hayashi track, the surface temperature (or effective temperature) is essentially constant while the luminosity decreases. The star heats up from the inside out since gas escapes the outer layers more easily. As the center becomes hotter, the opacity decreases and the convection zone slowly recedes. The star then leaves the Hayashi track and proceeds a radiative contraction on the *Henyey track*. This causes the decreasing luminosity trend to reverse and the star becomes more luminous. Eventually the core temperatures will be sufficiently high to trigger the proton-proton reaction, converting  $H$  into deuterium ( $^2H$ ) and thereafter  $^3He$ .<sup>1</sup>

As a result, a convective core is created. This will however disappear if the mass of the star is below  $1.1M_{\odot}$ , whereas stars of higher mass will burn hydrogen in the cores through the *CNO-cycle*. Accretion of mass continues on the pre-ms phase on a thermal timescale. Stars of masses larger than  $9M_{\odot}$  moves so quickly into the MS phase that they are unobservable on the pre ms due to the thick shell of accreting mass, while stars of masses between  $1.6-9M_{\odot}$  end their accretion of mass on the pre-ms. When the star begins burning hydrogen in full hydrostatic equilibrium it is born onto the *zero-age main-sequence (ZAMS)*. Stars below  $0.08M_{\odot}$  never reaches ZAMS because their internal central temperature never becomes high enough to fuse hydrogen to helium in equilibrium. Instead they become degenerate, and are known as *brown dwarfs*. Although stellar pulsations in brown dwarfs were theoretically

---

<sup>1</sup>The full proton-proton chain is not yet completed since the abundance of  $^3He$  is still too low to burn hydrogen in full equilibrium.

predicted by Palla & Baraffe (2005) these pulsations have not yet been detected (Aerts et al., 2010; Cody & Hillenbrand, 2014).

The ZAMS is where the star begins the life on the main-sequence where it spends 90 % of its life burning H to He. The computed solutions from this stage on can be seen on Fig. 3.2. The main sequence corresponding to the hydrogen burning in the core is defined as the phase between point 1 and 2. For all stars, the luminosity increases during this phase. The reason for this is that the hydrogen is converted into helium which causes the mean molecular weight to increase, which can be seen from

$$\mu \simeq \frac{4}{3 + 5X - Z}, \quad (3.11)$$

where X, Y and Z is the hydrogen, helium and metal fraction respectively. The outgoing pressure must then compensate for the increase in gravitational pressure from the overlaying layers. Since  $P \propto \rho T$  the core will start contracting to increase  $\rho$ . As a result of this contraction, gravitational potential energy energy is released, which further causes an increase in T (from the Virial theorem). Since the radiative flux is proportional to  $T^3$  the temperature will increase, causing the opacity to decrease since  $\sigma \propto T^{-3.5}$ . Thus, the photons can escape more easily, and the luminosity increases.

It is more complicated to explain the change in global parameters such as the effective temperature and radius. The radius increases in general as the star evolves, but the rate of this expansion is mass dependent. For stars that have low masses (close to  $1M_{\odot}$ ) expansion is slow and the increase in luminosity will lead to an increase in the effective temperature as well, while it is the opposite for stars with higher masses and higher expansion rates. They will expand faster than the effective temperature increases, and will therefore cool down.

When hydrogen abundances get sufficiently low in the core, the star reaches the *terminal-age main-sequence* (TAMS). Here, the core now consists of helium. For intermediate mass stars,a noticeable feature is the "hook" following the ms, also known as the *Henyey Hook* (not to be confused with the Henyey track). This is clearly depicted on Fig. 3.3 As these type of stars have convective cores, the energy production will decrease uniformly throughout the core. The star will attempt to compensate for this by increasing the central temperature and keep the energy production up, hence causing the core to contract. As a result of the contraction, gravitational potential energy is released, where half is converted to thermal energy, heating up the core and essentially shifting the evolution to higher effective temperatures. This phase is in the order of a few megayears, which is extremely fast evolution compared to the main sequence (in the order of  $10^{10}$  yrs. Therefore, studying a star in this exact phase is very difficult since a star can only be verified to be in this phase through modelling, as observations in color-magnitude diagrams cannot resolve it. From now on we will refer to this phase as the *post main-sequence contraction phase*. At this point most of the energy production still comes from nuclear reactions, and the gravitational contribution is small in comparison. It is surrounded by a region where temperature is still high enough to burn hydrogen, and

slowly establishes a *shell source*. This will however not be dominant until all hydrogen is exhausted. When this happens at point 3 on Fig. 3.2, the evolution is accelerated and the star is no longer in equilibrium. The contracting core will thus be accompanied by an expanding envelope, causing the effective temperature to decrease. This phase will be referred to as the *post- main sequence expansion phase*. The outer convection zone deepens until it reaches the layers where nuclear fusion has occurs (the core). This is marked as point 5 and is also called *first dredge up*.

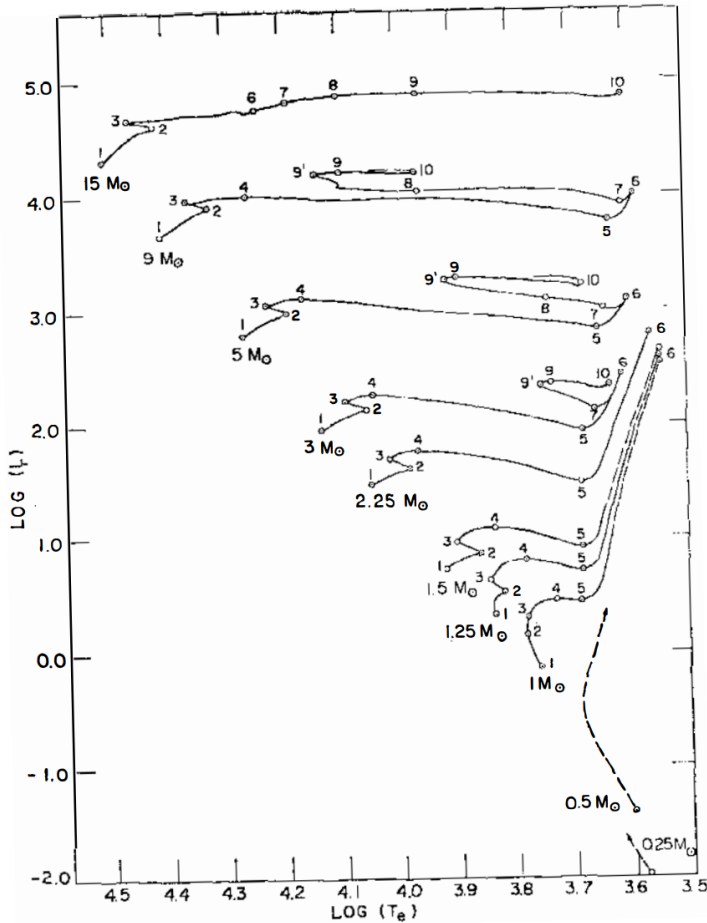


Figure 3.2: (Kippenhahn et al., 1990) Stellar evolution tracks of masses ranging from  $0.25M_{\odot}$  to  $15M_{\odot}$ . The numbers indicate different stages in the evolution. Figure from Iben Jr (1967).

At point 5-6, the star will then move back up the Hyashi track as a red giant. The further evolution from then is largely depending on the mass. Stars with masses between  $0.5 < M < 2.3M_{\odot}$  (relevant for this work) will have a degenerate helium core by the end of the main sequence (the exact cutoff depends on the initial metallicity in the star). The core contraction following the main-sequence continues until it reaches a temperature high enough to ignite helium in the core through the triple  $\alpha$  process. A thermal runaway known as *helium-flash* occurs and lifts the degeneracy of the helium core,

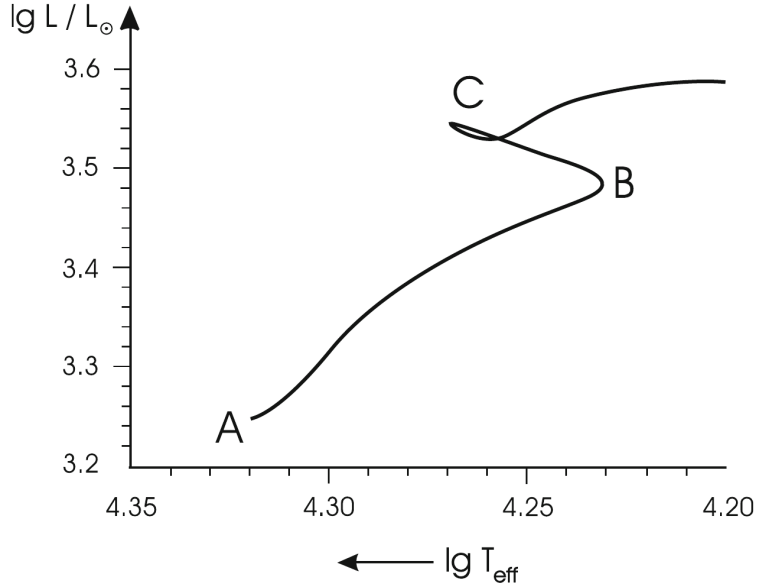


Figure 3.3: (Kippenhahn et al., 1990) Stellar evolution track of a  $5M_\odot$  star. The main sequence is marked between A and B, the post- ms contraction from B to C and the post -ms expansion is after C. Figure from (Kippenhahn et al., 1990).

settling the star down on the *horizontal branch* where it burns helium in the core and hydrogen in a shell (for stars with  $M < 2.0M_\odot$ ). Stars with masses below  $4-8M_\odot$  finish nuclear burning at carbon or oxygen. By the end, their envelopes will be ejected into space through stellar winds, forming planetary nebulae. Left behind is the remnant, a white dwarf star.

Now we have seen how a star's luminosity changes as a function of effective temperature throughout its evolution. As mentioned in the beginning of the chapter, assumptions on hydrostatic equilibrium and equation of state can provide us with solutions that relates several other properties. The numerical solutions to the radius  $R$ , surface gravity  $g$ , core density  $\rho$  and convective core mass are shown on Fig. 3.4 as a function of time. The red lines indicate the beginning of the ms, post-ms contraction and post-ms expansion phases, respectively. As for the radius, the star contracts for the entirety of the pre-ms. As it burns hydrogen on the ms it slowly expands (as the temperature in the core decreases slightly with time) until the post-ms where it again contracts. After hydrogen exhaustion the star undergoes fast overall expansion. Another parameter which is highly relevant for the frequencies is the surface gravity, as we shall see in Sec. 4. From theory we know that  $g \propto M/R^2$ , which is equivalent to the numerical results shown on Fig. 3.4. The density in the center increases rapidly on the Hyashi track when the star contracts, and follows the linear tendency  $\rho_c \propto \frac{3M}{\pi R^3}$  on the ms (by assuming  $\rho$  is a linear function of the fractional radius  $r$ . At the immediate post-ms phase it increases again as the core contracts rapidly.

An important parameter to also look at is the mass of the convective core. On the Hyashi track, the star is fully convective as it contracts. As the star burns hydrogen, the convective core mass slowly decreases until the point where . On Fig. 3.5, numerical results for the convective core mass ratio to the total stellar mass is plotted as a function of stellar age in Gyrs for tracks with different masses. It can here be seen that higher stellar masses leads to higher convective core masses. Since stars with higher mass also have shorter lifetimes on the ms, which is also well-depicted on the figure as the convective core mass drops to zero when nuclear fusion in the core ends, which occurs sooner for higher masses. At this point, the core will no longer have high enough temperature to be convective. The smaller window on Fig. 3.5 shows the convective core mass evolution on the pre-ms to the ms. Higher masses enter the hyashi track at a lower age than stars with smaller masses again indicating a faster evolution in general.

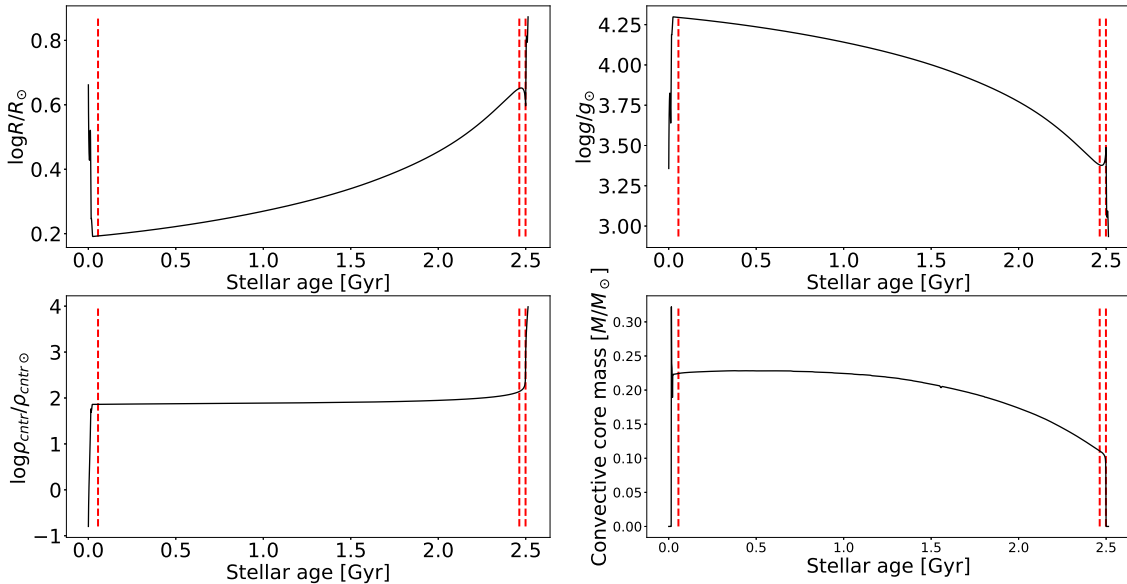


Figure 3.4: Numerically calculated stellar parameters for a track with  $1.75 M_{\odot}$ ,  $X=0.65$ ,  $Z=0.02$ ,  $\alpha_{mlt}=0.5$ ,  $\alpha_{ov}=0.3$ . The dashed lines marks the different stages of the evolution, leftmost being the beginning of the main-sequence, middle one the post- main sequence contraction phase and rightmost the post-main sequence expansion phase.

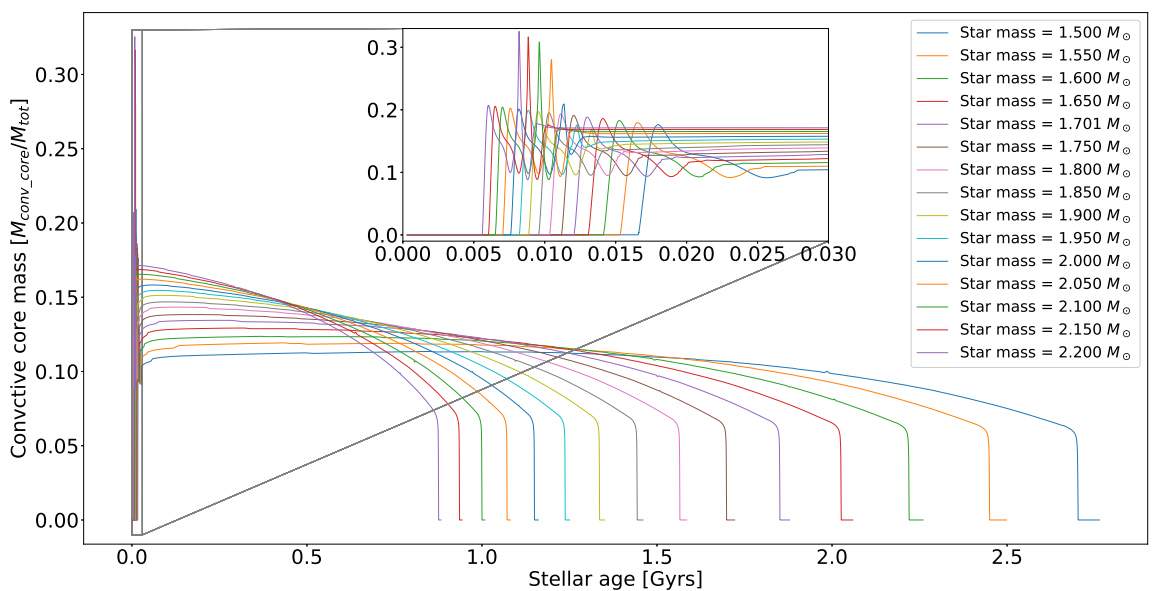


Figure 3.5: Numerical results for stars with masses ranging from  $1.5M_{\odot}$  to  $2.2M_{\odot}$ ,  $X = 0.70$ ,  $Z = 0.02$ ,  $\alpha_{mlt} = 0.5$  and  $\alpha_{ov} = 0.3$ . The convective core mass ratio is plotted as a function of stellar age. The small window shows a zoom in of the plot at the age where the convective core is established (on the ms)

# 4 An introduction to asteroseismology

The field of asteroseismology takes advantage of the pulsations in a star. All stars are different in structure, temperature, radius, luminosity, density and evolution. This is also what separates them from each other in a stellar oscillation spectrum, since it is unique to each type of pulsating star. Some stars oscillates on the pre-ms, others on the ms, and some on the Red Giant Branch. The nature of the oscillation spectra thus allows us to distinguish between stars with different interiors.

Pulsating stars contract and expands periodically, causing brightness changes that can be observed using two methods. 1) Changes in the velocity fields due to the periodic contractions and expansions gives rise to an observable Doppler effect which can be measured using spectroscopy. 2) Periodic brightness and thereby temperature variations causes variations in luminosity which can be measured with photometry. Observations can provide us with oscillation spectra allowing us to extract and identify the nature of each frequency. Modelling the star can then reproduce the environment in the star, specifically the sound speed which changes accordingly with the temperature and chemical compositions. Therefore, comparing these theoretically produced frequencies with observations allows us to estimate the properties in the star.

## 4.1 Stellar pulsations

Pulsations in stars is treated three-dimensionally, and assumes a spherical symmetry of the star (which is true when rotation of the star is too small to cause a distortion of the stellar symmetry). The three directions for which the natural oscillation modes have nodes are described by the distance to the center of the star,  $r$ , co-latitude  $\theta$  (measured from pulsation pole) and longitude  $\phi$ . Nodes are then defined as concentric shells of constant  $r$ , cones of constant  $\theta$  and finally planes of constant  $\theta$ . We can then describe the displacement in the  $(r, \theta, \phi)$  space as the following

$$\xi_r(r, \theta, \phi, t) = a(r) Y_l^m(\theta, \phi) e^{-i2\pi\nu t} \quad (4.1)$$

$$\xi_\Theta(r, \theta, \phi, t) = b(r) \frac{\partial Y_l^m(\theta, \phi)}{\partial \theta} e^{-i2\pi\nu t} \quad (4.2)$$

$$\xi_\Theta(r, \theta, \phi, t) = \frac{b(r)}{\sin(\theta)} \frac{\partial Y_l^m(\theta, \phi)}{\partial \phi} e^{-i2\pi\nu t}, \quad (4.3)$$

where  $a(r)$  and  $b(r)$  are the amplitudes,  $\nu$  is the oscillation frequency (1/Period) and  $Y_l^m(\theta, \phi)$  are the spherical harmonics given by

$$Y_l^m(\theta, \phi) = (-1)^m \sqrt{\frac{2l+1}{4\pi} \frac{(l-m)!}{(l+m)!}} P_l^m(\cos(\theta)) e^{im\phi}, \quad (4.4)$$

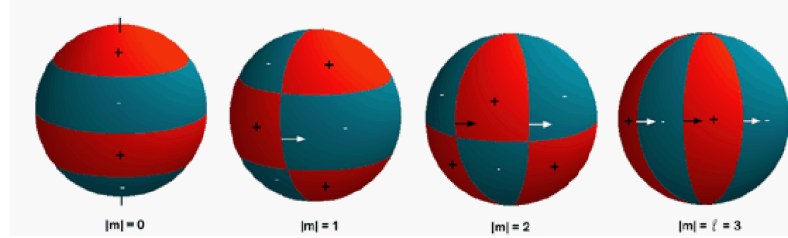


Figure 4.1: Possible geometrical nonradial pulsation patterns with  $l=3$  for a spherically symmetric star. The '+' indicates areas that move towards the observer, and the '-' away from the observer. From Antoci et al. (2011) (adapted from Wolfgang Zima 1999 master thesis.)

where  $P_l^m(\cos(\theta))$  are the Legendre polynomials<sup>2</sup>, with  $l$  being the spherical degree and  $m$  the azimuthal order. The normalization constant

$$c_{lm} \equiv \sqrt{\frac{2l+1}{4\pi} \frac{(l-m)!}{(l+m)!}}, \quad (4.5)$$

is defined such that the integral over the unit sphere of  $|Y_l^m|^2 = 1$ . Three quantum numbers describes the modes for 3-D stars,  $n, l$  and  $m$ .  $n$  is the *radial order* describing the number of radial nodes in the star.  $l$  is the *spherical degree* and represents the total number of surface nodes; finally  $m$  is the *azimuthal order* where  $|m|$  is the number of longitudinal nodes, crossing the equator. It then follows that  $l-|m|$  are the co-latitudinal nodes.  $m$  can vary from  $-l$  to  $l$ , yielding therefore a number of  $2l+1$  different nodes for each spherical degree. An example of all geometrical possibilities of an  $l=3$  mode can be seen on Fig. 4.1.

Generally we can divide stellar pulsations into radial and non-radial pulsations. Radial pulsations is the case for which  $l=0$ , with the very simplest geometry being the  $n=0$ <sup>3</sup> or *radial fundamental mode*. In this case there is a node only at the center with the corresponding anti-node at the surface, meaning that the entire star pulsates.  $n=1$  is the first radial overtone with one node,  $n=2$  the second overtone has two radial nodes and so on. If we assume that the star is uniform in temperature and chemical composition we would expect the ratio between the fundamental mode and the first overtone to be similar to that of an organ pipe, see Aerts et al. (2010). However, since we know that the temperature and chemical composition in the star changes with radius, we can exploit the fact that the sound speed changes accordingly, hence affecting the ratio. For instance we expect a ratio of  $F/1H = 0.77$  for  $\delta$ Scuti stars, but only  $F/1H = 0.71$  for Cepheids (as they are slightly more evolved). Hence, we can already say something about the interiors based only

<sup>2</sup>see Aerts et al. (2010) for more details.

<sup>3</sup>These equations are introduced for the sole purpose of presenting the spherical harmonics. They will not be used for calculations during the project. For more details, see (Aerts et al., 2010).

<sup>3</sup>Note that is also an issue of convention, as some groups prefer the lowest mode to be  $n=1$ . This is also the convention used in GYRE (discussed in Chap. 6)

on two observed frequencies. As for the non-radial modes, the *dipole* mode is the simplest with  $l = 1$ . They occur only for  $n > 0$ , e.i there will be at least one radial node in the star in this case.

As mentioned earlier we have assumed that the star behaves symmetrically, and that for non-radial modes all  $|m|$  values have the same frequency as the  $|m| = 0$ . However, if the rotation of a star is fast enough, it can cause the star to deviate from the assumption of spherical symmetry and lift this degeneracy such that all frequencies in  $m$  for a given  $l$  are different. The Coriolis and centrifugal forces will cause the wave to divert to either slightly lower or higher frequencies. Traveling with the rotation yields the *prograde* modes (lower frequencies), whereas traveling against rotation are *retrograde* modes (higher rotation)<sup>4</sup>. Assuming that the rotation still behaves uniformly we can write

$$\nu_{nlm} = \nu_{nl0} + m(1 - C_{nl})\Omega/2\pi, \quad (4.6)$$

where  $\nu_{nlm}$  is the frequency, and  $\nu_{nl0}$  is the unperturbed central frequency for which  $m = 0$ . The  $m = 0$  mode is the same even with rotation.  $\Omega$  is the angular velocity of the star and finally  $C_{nl}$  is the Ledoux constant- calculated from models (Aerts et al., 2010), Sec. 2.8. The result from this is that we get a multiplet with  $2l + 1$  components that *rotationally split* by  $(1 - C_{nl})\Omega/2\pi$ . However, the approximation of a uniform rotation of the star is rather crude. In reality rotation is asymmetric and the rotational splittings depend on several properties of the mode. Also, the components in the multiplet could be excited to different amplitudes or not excited at all. This complicates the identification of the multiplets severely. However, we are nonetheless able to observe these rotational splittings which is very relevant for fast rotating stars.

#### 4.1.1 Pressure and Gravity modes

Pulsations in stars can generally be divided into two groups: pressure modes (p-modes) and gravity modes (g-modes). The main difference between them is the restoring force in the two cases. In the pressure modes- the pressure is the main restoring force when a star is perturbed from equilibrium, whereas the g-modes have buoyancy as the restoring force. The difference between p-modes and g-modes is depicted on Fig. 4.2, where it can be seen that for p-modes, the gas moves vertically in contrast to the g-modes where the motion is horizontal. It is also possible to observe stars that shows both types of modes i.e. *mixed modes*. There is also a third option between p-modes and g-modes, which are the surface modes or f-modes. These only exist for  $l > 1$ . All three types of modes are shown on Fig. 4.2 as a function of spherical degree  $l$ .

There are two frequencies that constrains the area in which modes can propagate. The first is the *Lamb frequency*, describing the inverse time needed to travel a horizontal wavelength with local sound speed:

$$L_l^2 = \frac{l(l+1)c^2}{r^2}, \quad (4.7)$$

---

<sup>4</sup>The sign of the quantum number  $m$  indicates whether the mode is prograde or retrograde, depending on the convention used.

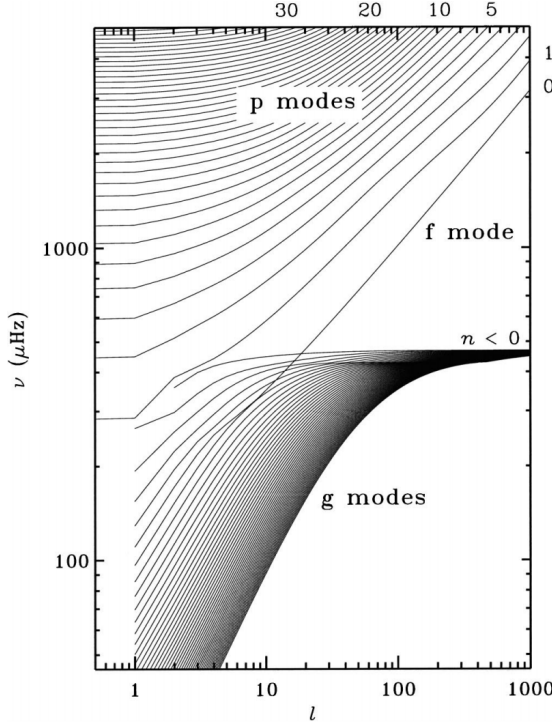


Figure 4.2: Frequencies of p and g-modes as a function of spherical degree  $l$  for a solar model. For p-modes, the frequency increases with overtone  $n$  and spherical degree  $l$ . For g-modes the it decreases with overtone, although it is a common convention to use negative  $n$  for g-modes in which case it will increase. Lines are chosen to illustrate the modes for clarity, but is should be noted that individual modes are discrete points. Figure from Aerts et al. (2010).

with  $l$  being the spherical degree and  $c$  the sound speed at radius  $r$ . The second frequency is the *Brunt-Väisälä frequency*. This is the frequency for which a fluent element oscillates around its equilibrium (vertically):

$$N^2 = g \left( \frac{1}{H} - \frac{g}{c^2} \right), \quad (4.8)$$

where  $H$  is the density scale height and  $g$  is the local gravity. Together these frequencies define cavities where a mode can oscillate:

- $\omega^2 > L_l^2$  and  $\omega^2 > N^2$  where  $\omega$  is the eigenfrequency mode. This region is situated in the outer layers of the star where the restoring force is pressure. Hence, oscillations in this area are the p modes.
- $\omega^2 < L_l^2$  and  $\omega^2 < N^2$  is the cavity for which the restoring force is buoyancy, hence pulsation modes propagates as g modes.

Energy from modes are mainly distributed to the layers whereas a pulsation can propagate, wheres outside the cavities the mode is damped or *evanescent*. The Brunt-Väisälä and Lamb frequency region is depicted in Fig. 4.3 for a post

main-sequence  $1.9M_{\odot}$  model. Left panels show the propagation diagram for three different stages of the star that are depicted on the evolutionary track on the right panels. In the propagation diagram the dimensionless frequency is plotted as a function of the fractional radius. The p-modes are located towards the surface of the star, with the cavity marked off with the red line. The cavity for g-modes is marked as a black line and peaks towards the center of the star.

Mixed modes exists in the overlapping area of the p-mode and g-mode cavities. They act as g-modes in the interior and p-modes in the outer layers. As the star becomes more evolved the modes change:

- There is a general increase in both p-modes and g-modes.
- The spacing between frequencies decreases as the star becomes more evolved.
- The cavity for g-modes grows in frequency and radius space. I.e. more evolved stars have more g-modes.
- The g-mode cavity will overlap the p-mode cavity more in evolved stars resulting in an increasing number of mixed modes.

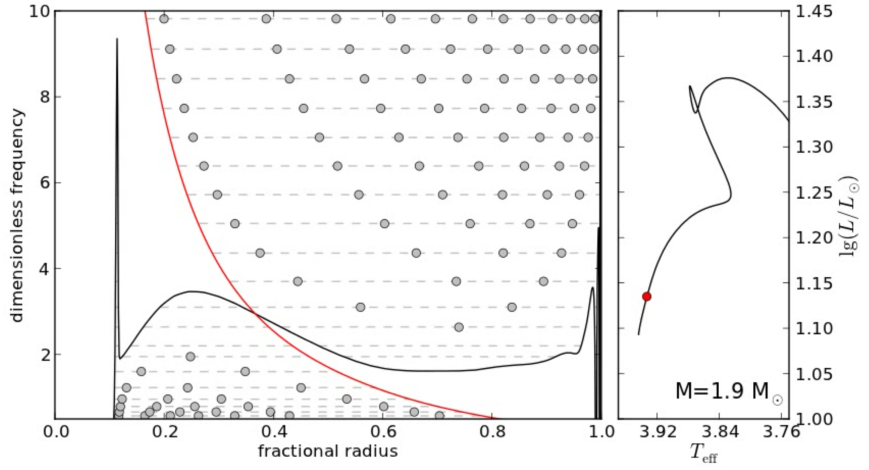
Since the frequencies in a star depends very strongly on the environment,i.e structure, they can therefore act as a tracer for the evolutionary stage of the star.

We can also exploit that different pulsation modes penetrates different layers of the stars. The depth which a mode will penetrate into is determined by the spherical degree  $l$ . Fig. 4.4 shows that the different *ray paths* for different spherical degrees. Dashed lines indicate the turning point where the wave front will be diverted back to the surface. Here, the mode frequency is equal to the local Lamb frequency. The wave is then reflected backwards again due to the drop in density in the outer layers. Besides from p-modes being more sensitive to conditions in the outer layers and for g-modes in the interior layers, there are two other important properties for p-modes and g-modes: 1) As the number of radial nodes increase, so will the frequencies of the p-modes, whereas the frequencies for g-modes will decrease. 2) for  $n \gg l$  there is an asymptotic relation for p-modes. This states that the modes are equally spaced in frequency. A similar relation exists for g-modes, however stating that modes are equally spaced in period.

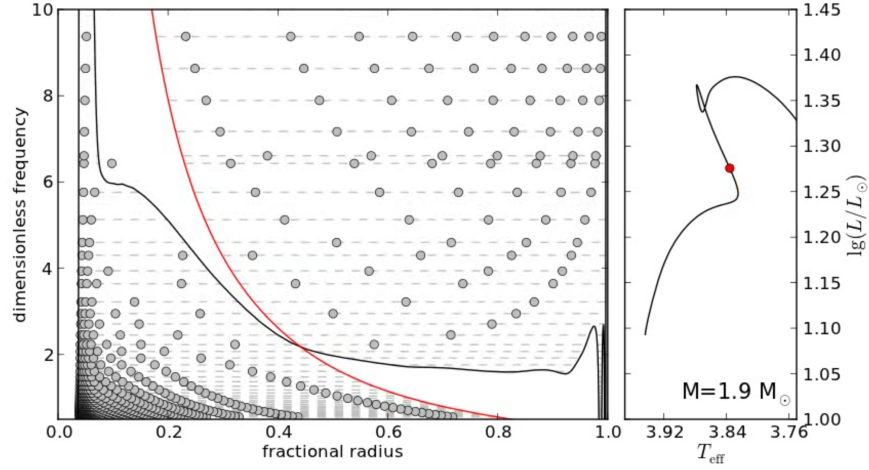
(Tassoul, 1980, 1990) used asymptotic theory to calculate the frequencies of p-modes as the following:

$$\nu_{n,l} = \Delta\nu \left( n + \frac{l}{2} + \tilde{\alpha} \right) + \epsilon_{n,l}, \quad (4.9)$$

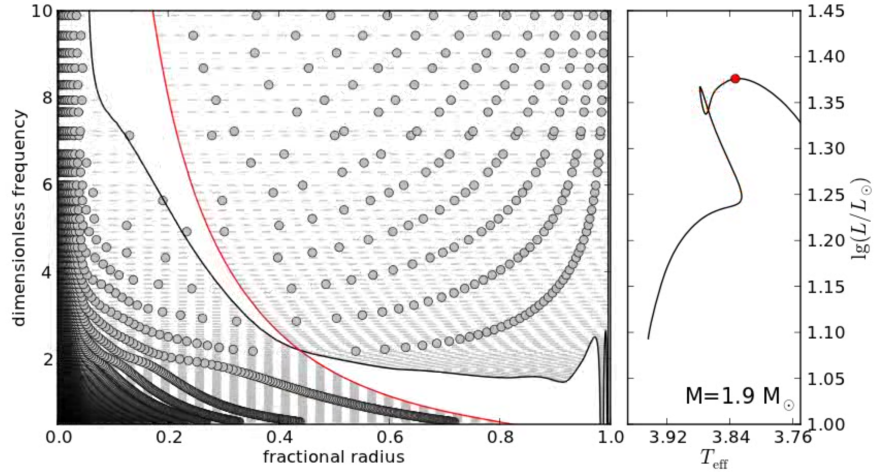
where  $n$  and  $l$  are the radial order and the spherical degree of the mode,  $\tilde{\alpha}$  is a constant of order unity,  $\epsilon_{n,l}$  is a small correction and finally  $\Delta\nu$  is *the large frequency separation*. This is the inverse of the sound travel time traveling from the surface to the core and back. It is given by:



(a) Frequencies of p- and g-modes on the ms.



(b) Frequencies of p- and g-modes on the post-0ms contraction phase.



(c) Frequencies of p- and g-modes on the post-ms expansion phase.

Figure 4.3: Left panels shows the propagation diagrams of p and g modes in a  $1.9 M_{\odot}$  star as a function fractional radius (0.0 being the center). Right panels shows the evolutionary track for the corresponding propagation diagram, with the current stage marked with a black dot. Credit Patrick Lenz.

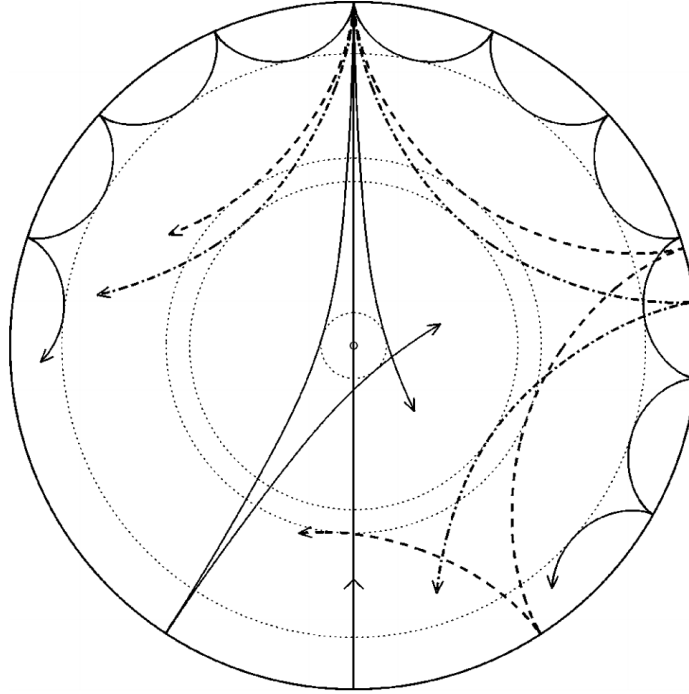


Figure 4.4: Schematic view of the propagating p-modes in a star. The rays penetrate the star to a depth depending on the spherical degree,  $l$ . The ray reaches a point where it will turn around. This is due to the increasing sound speed with depth. After the turnaround, the star will eventually be reflected near the surface, due to a fast decrease in density. The straight line shows the acoustic ray paths of  $l = 0, 2, 20, 25$  and  $7$ . From J. Christensen-Dalsgaard, 1997, the Theoretical Astrophysical Centre, Institute of Physics and Astronomy, Aarhus University.

$$\Delta\nu = \left( 2 \int_0^R \frac{dr}{c(r)} \right)^{-1} \quad (4.10)$$

where  $c(r)$  is the sound speed. It can be seen from this that this separation is sensitive to the radius of the star, and is thus a measure of the mean density.

The asymptotic relation for g-modes states that the periods of g-modes are given by:

$$\Pi_{n,l} = \frac{\Pi_0}{\sqrt{l(l+1)}}(n + \epsilon), \quad (4.11)$$

where  $n$  and  $l$  are radial order and spherical degree,  $\epsilon$  is a small constant and

$$\Pi_0 = 2\pi^2 \left( \int \frac{N}{r} dr \right)^{-1}, \quad (4.12)$$

where  $N$  is the Brunt-Väisälä frequency and the integral is over a cavity in which a given g-mode propagates.



## 5 The Delta Scuti stars

In this chapter we characterize describe the  $\delta Sct$  stars more in detail, including the stars used in this work.

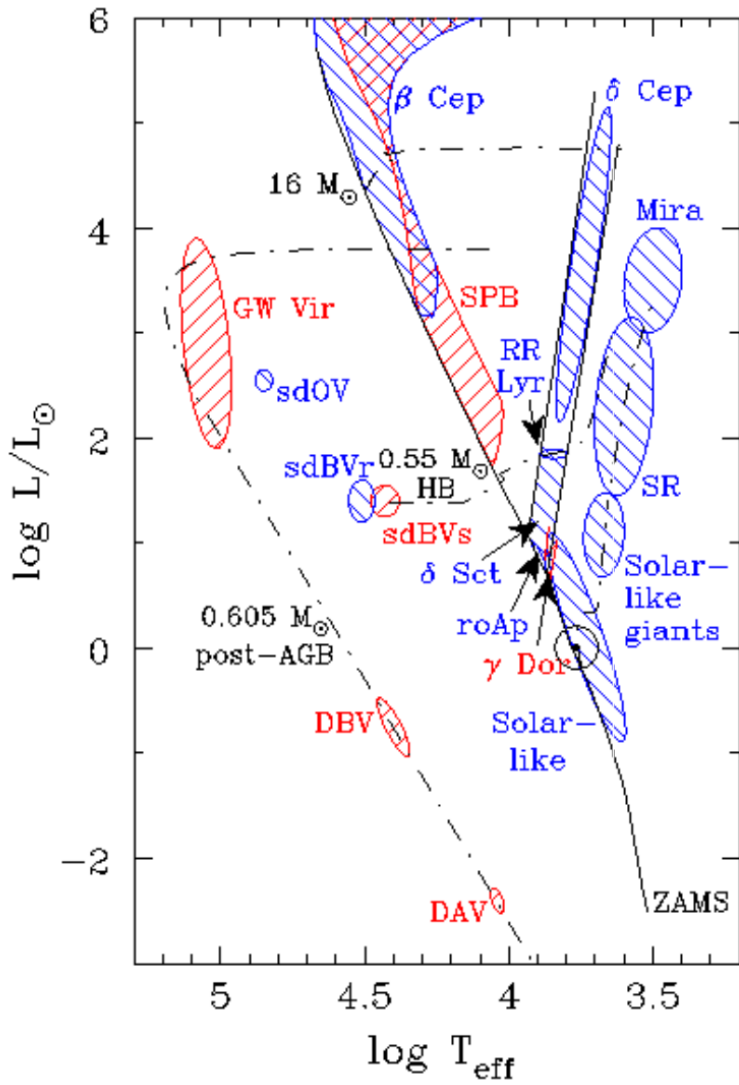


Figure 5.1: Asteroseismic HR-diagram, showing the different classifications of pulsating stars.

### 5.1 The pulsation HR-diagram and the driving mechanisms

As mentioned in the introduction, there are many different types of pulsating stars, situated over the entire Hertzsprung-Russel diagram (HR-diagram).

Fig. 5.1 illustrates the schematic overview of the various type in the *asteroseismic HR-diagram*. Stars that have p-mode pulsations are marked in red, whereas g-mode pulsators are blue. They range in the HR-diagram for which the various types pulsate are called their *instability strip*. Some stars can pulsate in both p and g-modes simultaneously. These types are called *hybrids*, and can be found where the instability strips overlap.

The type of oscillation a star pulsates with depends on the *driving mechanism*. For the Sun and solar like-oscillators the primary driving mechanism is the stochastic driving. Acoustic energy from motion in convective cells in the outer convection zone can sufficiently cause a resonance at the star's natural frequencies, where a part of the energy becomes oscillation modes. A mode will be excited in a convection cell and damped when the cell turn over. But since there is a large number of convective cells it will be re-excited immediately after at a different phase. So the excitation is random or *stochastic*. For  $\delta$  Sct stars, the driving mechanism is different. These are driven by a heat engine, which is a mechanism that transforms thermal energy in a star into mechanical energy of oscillations. When a star contracts the pressure and temperature increases, causing the opacity ( $\kappa$ ) to increase in layers of H and He ionization. The radiative flux from the core is hence blocked and builds up underneath the layers of higher opacity. When the star reaches a thermodynamic equilibrium the additional stored energy is transformed into mechanical energy, causing the layers to move beyond the equilibrium; the star expands. But the ionization of the gas causes a reduction in opacity and radiation can flow through. The gas then cools down so much that it can no longer support the weight of the overlying layers, and the star then contracts recombining H and He. The cycle then repeats itself. The zones where the radiative flux becomes trapped are the layers of partial ionization. The first zone is where H and He are ionized around 14.000 K, close to the surface of the star. Second ionization zone is around 40.000 K where He II is partially ionized. Lastly, the innermost zone is where ionization of iron elements occur, at 200.000 K. For  $\delta$  Sct stars the driving mechanism excites primarily in the He II ionization layer along with RR Lyrae and Cepheid stars.

Yet another type of driving mechanism is the *convective blocking* in Gamma Doradus ( $\gamma$  Dor), DA and DB dwarfs. This mechanism is similar to the  $\kappa$  mechanism, except the energy is stored in the outer convection zones. Such mechanism gives rise to g-modes oscillations rather than the p-modes from the  $\kappa$  mechanism.

Compared to the stochastic excitations in solar-like oscillators, the heat engine mechanism does not excite all modes to an observable amplitude, which makes *pattern recognition* impossible. It is also not well understood why only some modes are excited to an observable amplitude. (Dziembowski & Królikowska, 1990) suggested trapping in the acoustic cavity as an explanation to why only some modes are excited, but does not exclude the possibility that the process is random. Also, stars will only pulsate

## 5.2 Why Delta Sct stars?

The main focus of this thesis is the  $\delta$  Sct stars. In the pulsating HR-diagram  $\delta$  Sct pulsators are located in the lower part of *the classical instability strip*. As mentioned previously they pulsate due to the  $\kappa$  mechanism acting in the He II ionization zone within the region of the red and blue edges indicating the cool and hot edge of the instability strip. The location of these edges is defined by the effective temperature. Higher effective temperature means that the opacity bump will be located deeper in the star, yielding higher densities. Therefore, the blue edge indicates the maximum effective temperature for which the He II opacity bump is still located at densities where the  $\kappa$  mechanism can excite pulsations Pamyatnykh (2000). However, at temperatures lower than red edge the convective layers go deep enough that oscillations are damped. These boundaries were calculated theoretically by considering the interaction between pulsation and convection as described by (Grigahcène et al., 2005) with results published first by Dupret et al. (2004).

These are stars of spectral types from A0 to F2, with periods between 18 minutes and 8 hours. They can be found on the pre main sequence (PMS), main sequence (MS) and immediate post main sequence. They are so-called *intermediate mass* stars meaning that their masses range between 1.5 and 2.5 solar masses. There are several types of  $\delta$  Sct pulsators, but historically they are divided into two main groups: High-amplitude  $\delta$  Sct pulsators (HADS) with amplitudes of the dominant modes around the order of 0.3 mag. Radial pulsations are dominant for these types. A vast majority of these types have low projected rotational velocities. Low-amplitude  $\delta$  Sct pulsators (LADS) pulsate in many non-radial modes and are suggested to have higher projected rotational velocities with an average  $v \sin i$  of  $96 \text{ km/s}^{-1}$  (Solano & Fernley, 1997).

There are several reasons why these intermediate mass stars are of particular interest for understanding stellar evolution. They pulsate in a region of the HRD where many interesting physical processes occur. A fundamental and very important difference between these stars and the Sun is the structure, as described in Sec. 3. The classical instability strip indicates also where the transition between a deep convective layer with efficient energy transport by convection to a shallow convective envelope occurs. Additionally, stars in the classical instability strip have a convective core. Which gives rise to convective processes near the core that cannot be found in the Sun. The reason convection is so important is not only because it has an impact on the stability of pulsation but on the evolution of the star and particularly the lifetime. Therefore, understanding the processes behind these stars makes it possible to project that knowledge to stellar evolution in general. For studying the intermediate mass pulsators it is favorable if the  $\delta$  Sct star meets the following criteria:

- Every single additional pulsation frequency contain valuable information about the star. Therefore it is desirable to have a wide range of both radial and non-radial modes.

- As mentioned earlier, rotation causes numerous effects that needs to be taken into consideration both for mode identification (rotational splitting) and modeling.

For these reasons 44 tau is a good candidate for studying and modeling. The results and methods can then be applied to stars where mode id was less sucessfull and modeling is needed. In this study, this will be HD which will from now on be referred to as Superstar Antoci et al. (2014).

### 5.3 The delta Scuti stars 44 Tau and Superstar

The  $\delta Sct$  stars analysed in this work is shortly presented in the following section. Both stars are shown in

#### 5.3.1 44 Tau

44 tau is a class F2 IV  $\delta$  Sct star which lies in the intermediate mass region in the HR diagram.

Antoci et al. (2007) sums up the observational background and history of 44 Tau. Photometric campaigns were conducted by the *Delta Scuti Network* from 2000-2003. Here, an extensive frequency analysis was performed, and the rotational velocity has been determined to be as low as  $2 \text{ km} \pm 1 \text{ s}^{-1}$  (Lenz et al., 2008). Since the average projected rotational velocity of early F-type stars is  $114 \pm 5 \text{ km s}^{-1}$  (Royer et al., 2004), this is a very small value, which lead to the discussion if the star is a slow rotator or if it is observed pole-on (Antoci et al., 2007). An additional multisite campaign was initialized in 2004 (Zima et al., 2007) and Breger & Lenz (2008) contributed with frequency analysis from seasons 2004/5 and 2005/6, giving a total of 6 years of photometry data. This yielded a total of 49 frequencies. These frequencies are listed as presented in (Lenz et al., 2010) in Table 5.1. Zima et al. (2007) confirmed that 44 Tau is an intrinsically slow rotator by constraining the inclination angle to  $60 \pm 25^\circ$  with an equatorial rotation rate of  $3 \pm 2 \text{ km s}^{-1}$ . Atmospheric parameters were derived from spectroscopy to be  $T_{eff} = 7000 \pm 200 \text{ K}$  and  $\log g = 3.6 \pm 0.1$

No significant interstellar reddening has been found from these Strömgren indices. The metallicity was determined to be close to that of the sun by McNamara & Powell (1985). From this metallicity the Vienna NEMO grid (Model Grid of Stellar Atmospheres, Nendwich et al. (2004), Heiter et al. (2002)) can be employed to derive an effective temperature and surface gravity. This was done by Lenz et al. (2008), yielding  $\log T_{eff} = 3.839 \pm 0.007$  ( $6900 \pm 100 \text{ K}$ ), in agreement with the spectroscopic value. Based on the HIPPARCOS parallax of  $16.72 \pm 0.93 \text{ mas}$  a luminosity of  $\log L/L_\odot = 1.340 \pm 0.065$  was also derived. This was revised with a new bolometric correction to  $\log L/L_\odot = 1.305$  (Lenz et al., 2010).

The recent data release for the GAIA mission has provided new atmospheric parameters for both 44 Tau and HD 187547. GAIA data release 2 was released on 25 April 2018 and is available through the Gaia Archive (Brown et al.,

	Frequency [ $cd^{( - 1)}$ ]	$\sigma$ [ $cd^{( - 1)}$ ]	$A_y$ [millimag]	$(l, m)$	$A_w/A_y$
$f_1$	6.89802097	$2.762223525 \times 10^{-7}$	27.25	(0,0)	
$f_2$	7.00599425	$1.212730436 \times 10^{-6}$	6.206	(1,1)	
$f_3$	9.11743254	$3.311156496 \times 10^{-6}$	2.273	(1,1)	
$f_4$	11.5196319	$1.097910502 \times 10^{-6}$	6.855	(1,0)	
$f_5$	8.96062045	$8.454940424 \times 10^{-7}$	8.902	(0,0)	
$f_6$	9.56110274	$1.984809926 \times 10^{-6}$	3.792	(1,-)	
$f_7$	7.30312483	$1.648992107 \times 10^{-6}$	4.564	(2,0)	
$f_8$	6.7954641	$2.793833032 \times 10^{-6}$	2.694	(2,0)	
$f_9$	9.58283134	$4.381429983 \times 10^{-6}$	1.717	(0,0)	
$f_{10}$	6.33900993	$4.226006653 \times 10^{-6}$	1.781	(0,0)	
$f_{11}$	8.63914838	$5.442115161 \times 10^{-6}$	1.383	(0,0)	
$f_{12}$	11.2947181	$6.202960588 \times 10^{-6}$	1.213		
$f_{13}$	12.6914745	$1.844227733 \times 10^{-5}$	0.408		
$f_{14}$	5.30468666	$7.280114276 \times 10^{-6}$	1.033		
$f_{15}$	7.789734	$4.504308690 \times 10^{-6}$	1.671		

Table 5.1

2018). GAIA conducts three-band photometry on bright sources, assuming that they are single stars. From the three-band photometry, measured parallax, and training sets estimates on  $T_{\text{eff}}$  and  $R$  are made. The luminosity can be derived through the G-band magnitude  $M_G$  and bolometric correction  $BC_G$ :

$$-2.5 \log L = M_G + BC_G(T_{\text{eff}}) - M_{\text{bol}, \odot}, \quad M_{\text{bol}, \odot} \quad (5.1)$$

Some systematic errors were detected by Andrae et al. (2018). Estimates on the reddening and extinction are not applied in all cases due to non-reliable estimates. The GAIA atmospheric parameters for 44 Tau is listed along with the HIPPARCOS and spectroscopic values in Table ??.

	Value	Reference
$\log g$	$3.6 \pm 0.01$	(Zima et al., 2007)
$\log T_{\text{eff}}$	$3.839 \pm 0.007$	(Lenz et al., 2010)
$\log T_{\text{eff}}, \text{GAIA}$	$3.843^{+0.003}_{-0.007}$	(Brown et al., 2018)
$\log L/L_{\odot}$	$1.305 \pm 0.065$	(Lenz et al., 2010)
$\log(L/L_{\odot})_{\text{GAIA}}$	$1.383 \pm 0.004$	(Brown et al., 2018)

During this project, two difference runs will be made to implement the values for different parameters sets. Firstly, a run will be made with the Lenz et al. (2010) photometric  $T_{\text{eff}}$  and with the spectroscopic  $\log g$ . This will allow for a better comparison between the results. Second run will be made with the GAIA  $T_{\text{eff}}$  and  $\log g$  will be the same). In order to verify the GAIA values of  $\log g$ , a calculation was made based on the GAIA parallax, bolometric correction from Flower (1996) and B and V magnitudes from the Tycho-2 catalogue. This yielded a value of  $\log L_{\text{gaia}} = 1.3572 \pm 0.0082$ . This value will not be further

investigated in the runs, but is made for making the point that parameters from GAIA (or any other mission) should not be used without considering their reliability and updates.

Mode identification allowed to determine both the radial fundamental mode and the first overtone with confidence Lenz et al. (2008). Constraining models with these two frequencies has a major advantage in modeling, and Lenz et al. (2010) successfully reproduced all the frequencies using stellar evolution models from the Warsaw new Jersey code developed by combined with a stellar pulsation code (Paczynski, 1969). The best model showed that 44 Tau is on the post ms and more specifically in the contraction phase. Relative to the time spent on the ms for these stars, the lifetime in this phase is extremely short and therefore difficult to resolve in the HR-diagram. Hence, modeling is of great importance when studying the evolutionary stage of a star.

### 5.3.2 HD 187547

Like 44 Tau, HD 187547 is a detected  $\delta$  Sct. It was observed with the NASA spacecraft *Kepler* Koch et al. (2010). The first observations were taken over thirty days with one minute cadence. The frequency spectrum showed on Fig. 5.2, shows a large range of pressure modes for both high and low order radial modes, which could not be explained solely by the Kappa mechanism. Four different follow up ground-based observations were conducted during 2010 Antoci et al. (2011), mainly spectroscopy; see Antoci et al. (2011) supplementary material for more information. Initially, Antoci et al. (2011) interpreted the high radial overtones as being stochastically excited, and thereby reported Superstar as the first  $\delta$  Sct star where solar-like oscillations predicted by Houdek et al. (1999) and Samadi et al. (2002) were detected. However, an analysis carried out on an additional 960 days short cadence observations revealed that the spectrum is not consistent with a coherent signal either (Fig. 5.3), but is suggested to be related to turbulent pressure (Antoci et al., 2014).

The spectroscopic observations made by Antoci et al. (2011) led to estimates on the atmospheric parameters  $T_{\text{eff}} = 7500 \pm 250$ , surface gravity of  $\log g = 3.90 \pm 0.25$  and a projected rotational velocity of  $v \sin i = 10.3 \pm 2.3 \text{ km s}^{-1}$ . A photospheric metallicity of  $Z = 0.017$  was also derived. The analysis of the high-frequency modes lead to the determination of a large frequency separation of  $\Delta\nu = 3.5 d^{-1}$

	Value	Reference
$\log g$	$3.6 \pm 0.01$	(Zima et al., 2007)
$\log T_{\text{eff}}$	$3.839 \pm 0.007$	(Lenz et al., 2010)
$\log T_{\text{eff}}$ , GAIA	$3.843^{+0.003}_{-0.007}$	(Brown et al., 2018)
$\log L/L_{\odot}$	$1.305 \pm 0.065$	(Lenz et al., 2010)
$\log(L/L_{\odot})_{\text{GAIA}}$	$1.383 \pm 0.004$	(Brown et al., 2018)

Besides from the peculiar frequency spectrum, an analysis of the abundances of Superstar classified it as a chemically peculiar Am star. This means

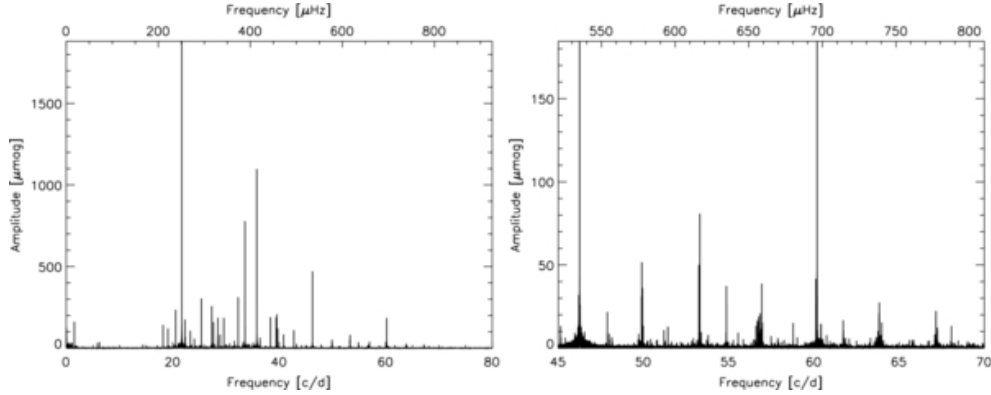


Figure 5.2: Fourier spectra of the Kepler short cadence data. Right panel: close-up in the frequency region interpreted by Antoci (2011) to be stochastically excited. Figure and caption from Antoci et al. (2014)

that it shows photospheric overabundances in Ba, Y, and Sr and underabundances in Sc and Ca (Preston, 1974). Particularly of interest are the pulsating AmFM stars, since they do not comply well with predictions from the Kappa mechanism. The theory states that settling of He causes an underabundance in the He II ionization layer, hence the Kappa-mechanism does not drive the pulsation sufficiently. Turcotte et al. (2000) implemented diffusion of heavy elements into the models to account for only a very tightly constrained instability region. However AmFm are not only observed in this region, but over the entire  $\delta$  Sct instability strip (Balona et al., 2011; Smalley et al., 2011). In that sense, Superstar is interesting not only because of its wide frequency range, but also because those frequencies are even more unusual for a pulsating Am star. Therefore it is of great interest to model this star to gain information on the nature of the pulsations.

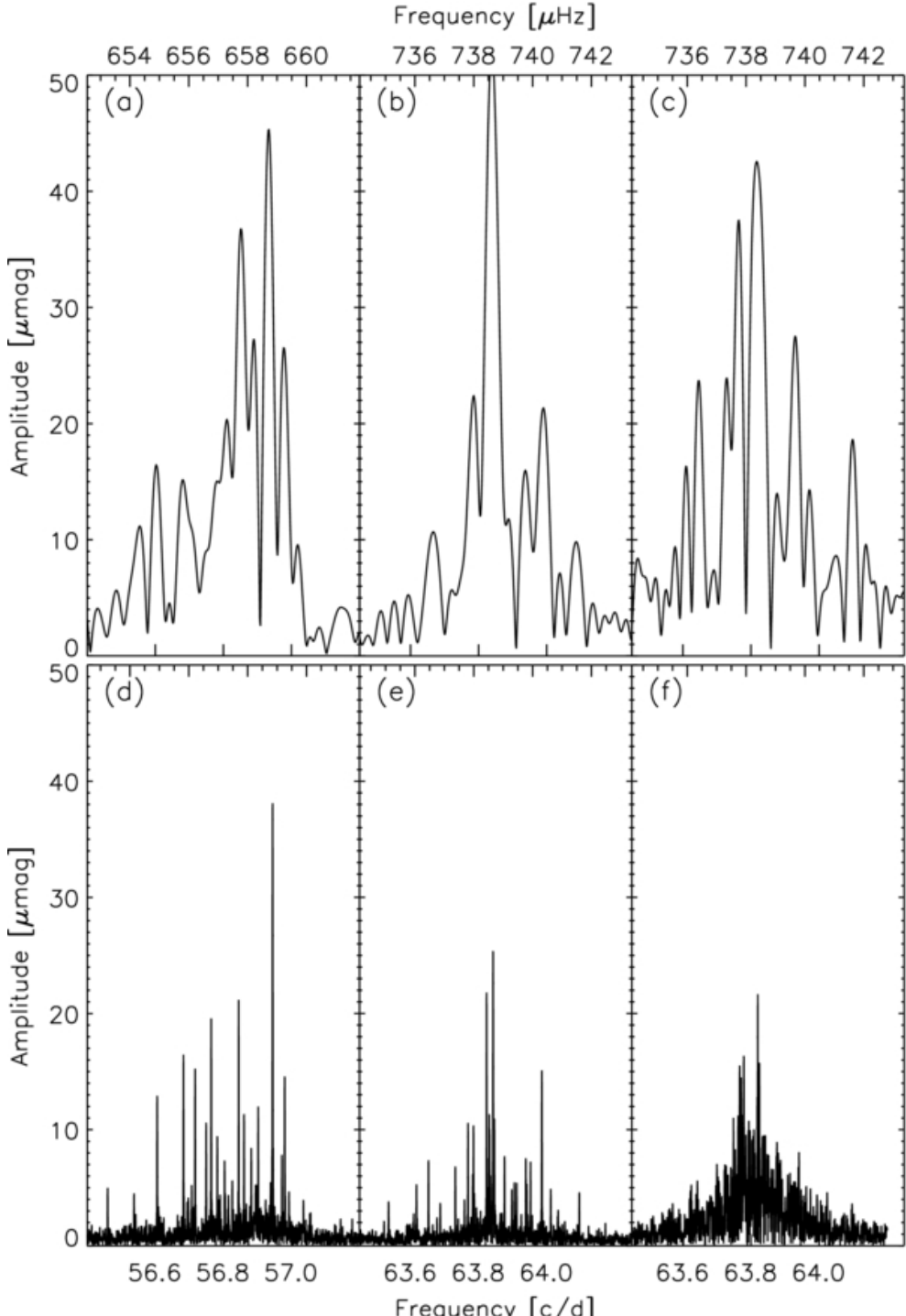


Figure 5.3: In panels (a), (b), (d), and (e), we show Fourier spectra of two oscillation modes observed in HD 187547 and interpreted by Antoci et al. (2011) as being stochastically excited. Panels (c) and (f) depict a simulated stochastic, damped, and re-excited oscillation mode. The Fourier spectra in panels (a), (b), and (c) are based on 30 days of observations (quarter 3.2), the same data set used by Antoci (2011). Panels (d) and (e) illustrate the oscillation spectra of HD 187547 based on 960 days of short-cadence data, clearly showing the temporally stable and well resolved peaks. For comparison, in panel (f) we show the Fourier spectrum of a simulated stochastically excited, i.e., non-coherent, mode with a mode lifetime of 2.8 days using the same duration for the time series as in panels (d) and (e). It can be seen that for a stochastic signal the amplitude decreases with increasing observing time, a characteristic we do not see for the coherent modes, unless beating due to unresolved peaks occurs as illustrated for the mode in panel (b) and (e). Figure

# 6 Computational tools

In this Chapter an introduction to the tools used to for computations of both stellar evolution models and pulsation frequencies is provided. In Sec. 6.1, the stellar structure and evolution code **MESA** is introduced, and the most relevant aspects for this work is discussed.

## 6.1 MESA

Modules for Experiments in Stellar Astrophysics or MESA is a suite of open source libraries that can be used to compute various applications in stellar astrophysics. Documentation can be found on the webpage <http://mesa.sourceforge.net/index.html> and from papers released with new updates (Paxton et al., 2013, 2015, 2018, 2019, 2010). MESA consists of several modules that works together in order to create computational models of stellar astrophysics. They have both the ability to work independently and each is constructed as a separate Fortran 95 library. All original modules (Paxton et al., 2010) with their purposes are listed in Table 6.1.

Here, the main focus will be on the **MESA star** 1D stellar evolution module, and the modules implemented in relation to controlling the run, such as **MESA kap**.

There are several modules that provides numerical methods used for the computations, the first being the **mtx** module, providing an interface for linear algebra and matrix manipulation. The **num** uses these matrix routines as well as providing a number of solvers for ordinary differential equations form Wanner & Hairer (1996). It also includes a Newton-Raphson solver for multidimensional, nonlinear root finding (derived from Lesaffre's version of the Eggleton stellar evolution code (Eggleton, 1971; Lesaffre et al., 2006; Pols et al., 1995). The modules **interp\_1d** and **interp\_2d** uses 1-dimensional and 2-dimensional interpolation, respectively. Lastly, the **alert** module reports messages and errors and the **utils** module checks the variables for bad numbers such as NaN and infinity.

### 6.1.1 Stellar structure and evolution

The **MESA star** module that implements several numerics and astrophysics modules to compute stellar evolution tracks using a Henyey-style code (Henyey et al., 1959) with automatic mesh refinement, analytical Jacobians and solutions to coupled stellar structure and composition equations. The **MESA star** implementations is vastly constructed with inspiration from stellar evolution and hydrodynamics codes such as EV (Eggleton, 1971), EVOL (Herwig, 2004), EZ (Paxton, 2004), FLASH-the-tortoise (Lesaffre et al., 2006), GARSTEC (Weiss & Schlattl, 2008), NOVA (Starrfield et al., 2000), TITAN (Gehmeyr & Mihalas, 1994) and TYCHO (Young & Arnett, 2005).

Firstly, **MESA star** reads the input files needed for the run. These are two files determines the specific controls for **MESA star** to read and implement.

Name	Type	Purpose
<code>alert</code>	Utility	Error handling
<code>atm</code>	Microphysics	Gray and non-gray atmospheres; tables and integration
<code>const</code>	Utility	Numerical and physical constants
<code>chem</code>	Microphysics	Properties of elements and isotopes
<code>diffusion</code>	Macrophysics	Gravitational settling and chemical and thermal diffusion
<code>eos</code>	Microphysics	Equation of state
<code>interp_1d</code>	Numerics	One-dimensional interpolation routines
<code>interp_2d</code>	Numerics	Two-dimensional interpolation routines
<code>ionization</code>	Microphysics	Average ionic charges for diffusion
<code>jina</code>	Macrophysics	Large nuclear reaction nets using reaclib
<code>kap</code>	Microphysics	Opacities
<code>karo</code>	Microphysics	Alternative low-T opacities for C and N enhanced material
<code>mlt</code>	Macrophysics	Mixing length theory
<code>mtx</code>	Numerics	Linear algebra matrix solvers
<code>net</code>	Macrophysics	Small nuclear reaction nets optimized for performance
<code>neu</code>	Microphysics	Thermal neutrino rates
<code>num</code>	Numerics	Solvers for ordinary differential and differential-algebraic equations
<code>package_template</code>	Utility	Template for making a new MESA-module
<code>rates</code>	Microphysics	Nuclear reaction rates
<code>screen</code>	Microphysics	Nuclear reaction screening
<code>star</code>	Evolution	One-dimensional stellar evolution
<code>utils</code>	Utility	Miscellaneous utilities
<code>weaklib</code>	Microphysics	Rates for weak nuclear reactions

Table 6.1: MESA module Definitions and Purposes. From (Paxton et al., 2010).

The first file specifies the type of evolutionary calculation, EOS and opacity prescriptions, and chemical composition amongst other properties. Changing the parameters in this file allows to make a grid as described in Sec. 7.1. The second file specifies the controls to be applied during the run All of the options for the inlist files can be found in the documentation. There are generally two ways to initiate an evolutionary run. One option is to let MESA a PMS model based on an input of an input mass, luminosity and initial abundances. The star then evolves from the PMS and until a stop criterion is fulfilled. However, if an entire grid is needed it is a disadvantage to have to calculate all the PMS models for all individual tracks. The second (and more favorable) option in this work, is to reuse a pre-calculated PMS model in the inlist and let MESA relax the parameters in the following evolution. In this work a  $1.7M_{\odot}$  PMS model is applied for this purpose. However, one needs to be aware that relaxing the parameters can give numerical issues if the PMS sequence model and the initial parameters used for further evolution are too far apart (since it would be numerically feasibly to relax the mass of a  $1.7M_{\odot}$  model to  $8M_{\odot}$ ). However, the grid calculated in this work (see Sec. 7.1) combined with the  $1.7M_{\odot}$  PMS sequence model only poses numerical issues for a few tracks, see Sec. 7.1.

When the input files have been read, the physics modules (EOS, opacities and nuclear network) are initialized. In the first step, the evolutionary run has then begun. MESA then continues the evolution by continuing to the next timestep. As this happens, the model is remeshed if necessary, mass loss is taken into account (although not used in this work since the mass is assumed constant after being relaxed to the MS), abundances are adjusted by taking diffusion into account, and calls the solvers (Newton-Raphson) to obtain a new structure and composition solution. Lastly, a new timestep is calculated. Within this one timestep, **MESA star** builds a one-dimensional spherically symmetric model, where the star is divided into cells reaching from the core to the surface of the star. During one timestep, **MESA** does not solve structure equations separately from composition equations. Instead, an entire set of coupled equations are solved for all cells simultaneously. Some of the controls for adjusting structure and timesteps relevant for this work further discussed in Sec. 7.2.

### 6.1.2 Output

There are three different types of output files in MESA, which can be used for different purposes. The first is the *history* file, where the history for the entire run is saved. Whereas the header contains information on the initial parameters set in the run such as the initial mass and Z abundance. Hereafter, one line corresponds to one *model*. The first two columns contain information on the *model\_number*. The rest of the columns show calculated properties such as age, mass and luminosity.

The next output file is the *profiles*. On the contrary to the history files, the profiles only contain information of one model. The first line shows the global properties such as the age. The rest of the file shows properties for each point or *zone* in the model. Since it is computationally heavy for MESA to write the profiles, it is necessary to evaluate whether all zones are needed in the output files. For this project, it was found sufficient to only use information on the core and surface.

The third output file is the *profiles.index*. Since MESA does not save profiles for every *step*, the *profile number* and model number are not necessarily the same. Therefore, the *profiles.index* tells the user how to translate between these.

Additionally, in order to be able to calculate the frequencies in GYRE, an output file for this is needed. This is done with the `write_pulse_data_with_profile = .true.`, producing a *profile.GYRE* file for each corresponding profile. These will be described in more detail in Sec. 6.2.

### 6.1.3 Convection treatment

In Sec. 3.1 the condition for convection has already been discussed briefly. There are several theories that lead to a numerical implementation. Therefore, the main focus here will be the implementation of **MESA mlt** module.

The implementation of convection in both **MESA** and the Warsaw-New Jersey stellar evolution code is based on the standard-mixing length theory

of convection as presented by Weiss et al. (2004). This theory provides a very simplified picture of the physical processes of convection, as well as a qualitative and reasonable description of heat transfer by convection. However, the quantitative results should not be expected to have high accuracy or reliability. One parameter that particularly causes discussions due to its high uncertainty, is the parameter describing the mixing length itself. The mixing length,  $\Lambda$  is described as the mean-free path that a fluid element travels inside a convectively unstable region in a star. In outer layers of a star, it can be assumed that  $\Lambda$  is proportional to the pressure scale height  $\lambda_p$ . In **MESA** `mlt`, the mixing-length is therefore implemented as

$$\Lambda \equiv \alpha_{mlt} \lambda_p, \quad (6.1)$$

where  $\alpha_{mlt}$  is the parameter input in **MESA**. It is generally assumed to be constant throughout the star, nor is it dependent on mass or evolution. The value of this parameter is only known to be of order one (while the default value in **MESA** is 2), from physical arguments. Having a high mixing length in outer layers essentially means that the bubbles can travel far before dissolving into the environment, i.e. the convection is efficient. For  $\delta$  Sct stars, the convective outer layer is significantly smaller than that of solar-type stars. Therefore, it is safe to assume smaller efficiency of energy transport by convection. On Fig. 6.1, evolutionary tracks for two models with different mass can be seen in an HR-diagram. The black line shows the track calculated with  $\alpha_{mlt} = 0.2$  and the red with  $\alpha_{mlt} = 0.8$ . From this it is clear that the dependence on the mixing-length parameter is not very significant until just before the red giant branch. Here, the higher  $\alpha_{mlt}$  causes a significant drop in luminosity. This is because the convective layer of the star deepens as it moves closer towards the red giant branch, meaning that energy transport convection dominates over radiation. A higher value of  $\alpha_{mlt}$  thereby has a larger effect at this stage as it causes an increase in convective efficiency (hence a decrease in energy transport by radiation) and a drop in luminosity.

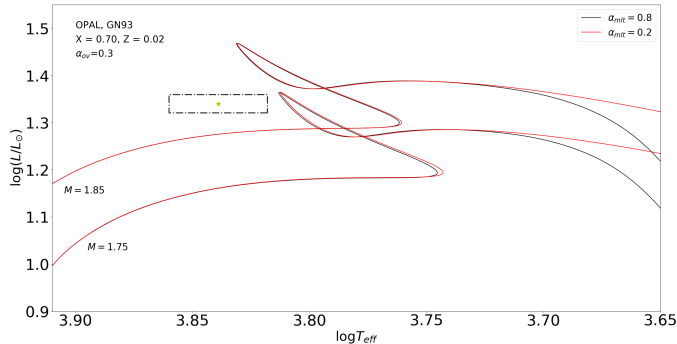


Figure 6.1

Even though the mixing length paints a nice picture of the convection in the outer layers, there are still issues related to the convection deep in the interior.

Specifically to which extend chemical elements are mixed, as it has a big impact on the later evolution of the star. For main-sequence stars with a convective cores the main problem is the convective core overshooting. The convective core overshooting relates to the issue that the boundary between convective core and radiative layers is not sharp; instead, the convection "overshoots" into the layer above (for a quantitative description, see Kippenhahn et al. (1990), Chap. 30). The amount of overshoot depends on the velocity of the convective elements and the breaking force, which are difficult to find as it includes non-local solutions to velocities, gradients and fluxes in the entire core. Therefore, the values for overshooting are, as for the mixing length), arbitrary and can only be evaluated through modeling.

There are two standard methods that are commonly used to calculate the overshoot numerically. The first one is quite similar to that of the mixing length, describing the extension of the convective region defined by the Schwarzschild criterion, in terms of pressure scale height

$$l_{ov} = \alpha_{ov} H_p, \quad (6.2)$$

in which  $\alpha_{ov}$  is typically in the order of 0.1 and 0.2. Even though it resembles the description of the mixing length parameter  $\alpha_{mlt}$ , it has no relation to it and is purely determined through comparing models to observations. This prescription is applied as "step overshoot" in MESA. The second method considers convective overshoot as a diffusive process with a diffusion constant depending on the radial distance  $z$  from the border defined from the Schwarzschild criterion.

$$D(z) = D_0 \exp \frac{-2z}{f_{ov} H_p}, \quad (6.3)$$

where  $f_{ov}$  is a free parameter in the order of 0.02, and  $D_0$  sets the scale of the diffusive speed. This prescription has a particular advantage as it can be added quite easily to a stellar evolution code where diffusion is already implemented. However, for this work, only the former prescription is implemented.

The reason that convective core overshoot is important to implement is that the overshoot causes extra mixing of elements. Hence, more hydrogen is transported to the core, acting as additional fuel on the main sequence. Therefore, just a small extension to the convective core causes a significant continuation of the main sequence. An example can be seen on Fig. 6.2, where two stellar evolution tracks of masses  $1.95M_\odot$  and  $1.75M_\odot$  are shown. The black line indicates the track with  $\alpha_{ov} = 0.2$  and the red line the corresponding track with  $\alpha_{ov} = 0.3$ . It can here clearly be seen that the main sequence is significantly longer for models with higher  $\alpha_{ov}$ , and that it affects the remaining part of the evolution as well.

#### 6.1.4 Element abundance mixtures

In order for MESA to calculate a stellar model, the element abundances needs to be implemented. The chemical composition of a star is assumed to be a reflection of the distribution of elements in the cloud from which the star was born, assuming that the composition is preserved in the outer layer of the star.

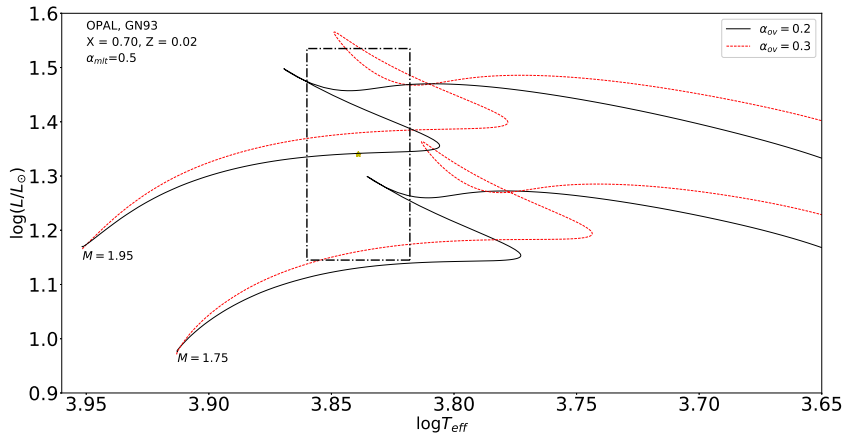


Figure 6.2

Since solar neighbourhood abundances are usually more accurately measured than stars outside, the solar element mixture is commonly used for modeling stars from outside the neighbourhood as well. In MESA, the initial abundances X (hydrogen), Y (helium) and Z (metals, i.e. all elements with atomic numbers higher than helium) is given in terms of mass fractions where  $1 = X + Y + Z$  must always be fulfilled.

The solar element abundances depends on the choice of theoretical atmosphere model. Hence, they are updated continuously as atmosphere models are changed and improved. There are several abbreviations of element mixtures that can be applied in MESA, such as GN93 (Grevesse & Noels, 1993), GS98 (Grevesse & Sauval, 1998) and a09 (Asplund et al., 2009). The most commonly used solar element abundances are GN93. The solar mass fractions for these abbreviations are given in Table 6.2.

Abbreviation	X	Y
GN93	0.70	0.02

Table 6.2: Solar element abundances for the most common abbreviations in MESA. The mass fractions X and Z are the estimated solar values.

Grevesse & Noels (1993) used a one-dimensional hydrostatic atmosphere model to derive the solar abundances, and compared to the solar system abundances extracted from meteorites, and found good agreement. This has been the most commonly used standard element mixture used for modeling, and in this project, only the GN93 element mixture is applied. However, the importance of element mixture choice is further discussed in Sec. 8.

### 6.1.5 Equation of state

The equation of state takes the density and temperature and calculate the corresponding pressure, ionization degrees and thermodynamic quantities necessary to calculate the stellar structure.

The equation of state is implemented through the `EOS` module, where density  $\rho$  and temperature  $T$  are treated as independent variables in the Helmholtz free energy formulation. However, some calculations are carried out through the Gibbs free energy formulation where the density can be provided through root-finding. This is computationally heavy, so the roots are therefore pre-processed, creating  $P_{gas}$  and  $T$  tables that allows for a quicker solution when calling the `EOS` module (provided that the input values are within the range of the pre-computed values). The  $\rho - T$  tables are based on OPAL EOS tables from Rogers & Nayfonov (2002), and for lower values Saumon et al. (1995), covering an area up to  $Z \leq 0.04$ . If parameters are outside of the region covered by the MESA tables, the EOS from HELM (Timmes & Swesty, 2000) and PC (Potekhin & Chabrier, 2010) are used. These use a free energy approach assuming complete ionization, which is applicable to the region outside of the tables (where cooler stars are only partly ionized).

### 6.1.6 Opacity data

From the density, temperature and chemical composition, the `EOS` yields estimates on the ionization equilibrium concentrations and level populations in a medium. These can be used to evaluate the Rosseland mean opacities. These are implemented though the `kap` module in `MESA`, where pre-processed opacity tables are within the `make_kap` module. The electron conduction opacity tables are based on Cassisi et al. (2007). For the radiative opacities, low temperature regions ( $\log T \leq 4$ ) is covered by Freedman et al. (2008) or Ferguson et al. (2005).

## 6.2 GYRE

In order to interpret asteroseismic observations from recent mission such as MOST (Matthews, 2007; Walker et al., 2003), CoRot (Michel et al., 2008) and Kepler (Borucki et al., 2009; Gilliland et al., 2010), a stellar oscillation code calculating the eigenfrequency spectrum of an input stellar model is needed. The asteroseismic module included in `MESA` is based on the stellar pulsation code `ADIPLS` (Christensen-Dalsgaard, 2008a), which allows for a calculation of the eigenfrequencies. However, a demand for more detailed non-adiabatic calculations lead to the development of `GYRE`, which is an open source pulsation code from 2013 described in (Townsend et al., 2017; Townsend & Teitler, 2013) and on the webpage (Townsend, 2013).

`GYRE` is written in `Fortran 2008` and uses a *Magnus Multiple Shooting*(MMS) scheme to solve linearized pulsation equations. The following steps are used to calculate the eigenfrequencies for an arbitrary input model:

1. *Stellar model* As a first step, `GYRE` needs to read an input model. This model can be either read from a pre-built or can be constructed analytically. It supports three different classes of models. The first is the evolutionary models (which is what is use in this work) constructed from a stellar evolution code. The second relies on polytropic models, and

the last is purely analytical calculations based on explicit expressions for structure coefficients.

2. *Grid calculation* When the file has been read, a calculation grid is constructed. The grid allows for multiple shooting and eigenfunction reconstruction. The type of grid depends on the type of input model.
3. *Root-finding* Initial guesses for discriminant roots are found by scanning the frequency space in the grid.
4. *Eigenfunctions* Based on the initial guesses of roots, the corresponding eigenfunctions are then constructed.

These are only the very basic steps used by **GYRE**; a more detailed description of the numerical steps used is beyond the scope of this work, and the reader is instead referred to (Townsend & Teitler, 2013).

It is now also possible for **GYRE** to be implemented directly in the **MESA star** module, which allows for a fully automatic calculation of both stellar evolution and frequencies. However, implementing it is a bit more intricate than reading in the files separately; therefore, the first method is used in this project, simply calculating a grid of models that can then be used as an input for the **GYRE** calculations.

### 6.2.1 Input and output options

**GYRE** reads input parameters given in an input file. The input file is structured in a similar way as the **MESA** inlist files, consisting of several namelist groups:

- *Constants* Defines the physical constants such as the gravitational constant and solar parameters (mass, luminosity etc.)
- *Stellar model* Defines the stellar model that **GYRE** reads and constructs eigenfrequencies for.
- *Mode parameters* Defines mode parameters such as l,m and minimum and maximum radial orders.
- *Oscillation parameters* Defines the parameters relates to the oscillation, such as inner and outer voundary conditions and rotation.
- *Numerical parameters* Specifies numerical methods parameters.
- *Frequency scan* Defines the span of the frequency space scan with a set of points.
- *Calculation grid* Defines the parameters used for the calculation grid.
- *Output files* Specifies how the output produced by the end of a run. This can be the file format, frequency units, comma separation etc.

For this project, the input model is constructed as a .GYRE file for every profile constructed in **MESA**, which is then read into the **GYRE** input file. The input files used in this project for 44 Tau and Superstar is constructed from a bash script which can be found on ...([link to git](#)). When the input file has successfully been read and the calculations have finished, **GYRE** constructs one of two different types of ouput files. The first is the Summary files that provides global information on the theoretically produced modes. The second is the mode files, containing information on a single mode including detailed eigenfunction quantities such as rotation kernels. For this project, the first file is used. The contents of the output file is defined in the input file described above with the **summary\_item\_list** (or, correspondingly **mode\_item\_list**). The most relevant for this project is the harmonic degree, radial order and frequencies.

Several options for non-adiabaticity can be included in the **GYRE** calculations. This has the advantage that it yields the excited frequency range which can be compared to observations. One of the major contradictions between observations and theory in asteroseismology is that theory predicts all frequencies to be excited if the pulsations are driven by the kappa mechanism. But unfortunately, this is not what is observed, Therefore, using non-adiabatic calculations can provide a more detailed information on the excitation of each mode. However, the major disadvantage of this is that since non-adiabatic equations rely on solving non-linear equations, the calculation time increases significantly from that of adiabatic calculations. Especially if it needs to be done for an entire grid. Therefore, this option is not used in this work.



# 7 Modeling 44 Tau and Superstar

In this chapter the process of modeling the stars 44 Tau and Superstar in MESA and GYRE is described. The methods for comparing the models to observations is introduced and discussed.

## 7.1 Choosing a grid

For this project models are created in order to compare to observations and ultimately narrow down the parameter space for 44 Tau and HD 187547. More than one approach can be taken in order to reach this goal, each with their own advantages and disadvantages. (Lenz et al., 2010) narrows down the grid size by first calculating the best mass for each stage. I.e. it is an approach where the star is assumed to be in either ms, post-ms contraction or post-ms expansion phase, and these results in three different grids where the best model is found for each stage. This method has the advantage that is it forces a result on all the relevant possibilities. However, it is a process that requires the grid to be narrowed through several steps, including a separate analysis of the mass range.

In this project, a slightly different approach is used. Instead of dividing the models into different stages and narrowing it down, a wide grid stretching over the entire instability domain is calculated, and of these the best models are found. To find not only the best overall model, but also consider their tracks and initial input parameter combination, the best model for each track is found. This choice is discussed in Sec. 7.3.1.

As discussed in Sec. 6, the initial set of parameters chosen has a great influence of the further evolution of the star. Therefore, a grid needs to be chosen with care in order to get a big enough grid to not only cover the observationally determined parameter space, but adequately beyond this in order to include the uncertainties on the observations. Since the mass has not been observationally determined, a good place to start is the instability strip. Usually, the intermediate mass stars have masses between  $1.5\text{--}2.5 M_{\odot}$  in order to cover the strip where pulsations are expected. Therefore this mass range is chosen to be from  $1.5M_{\odot}$  to  $2.2 M_{\odot}$ , where the most important part is to include masses all the way down to  $1.5M_{\odot}$  since these star in particular mark the transition to convective cores. The initial abundances are chosen to be within the numerical boundaries of MESA, as discussed in Chap. 6. This yields a range of  $0.65 < X < 0.70$  and  $0.01 < Z < 0.03$ . Numerical results for two different masses and  $Z$  can be seen on Fig. 7.1. Here, the red color correspond to masses of  $M = 1.75M_{\odot}$  and black lines  $M = 1.85M_{\odot}$ . The different values of  $Z$  are represented with full and dashed lines respectively. There is a clear difference between tracks with different  $Z$ . Higher values of  $Z$  yields a high opacity which blocks the radiation from the inner layers. Hence, stars with

higher metallicity will be less luminous. In this case, the luminosity difference is in the order of  $\approx 0.2$  within the three sigma uncertainties on the luminosity.

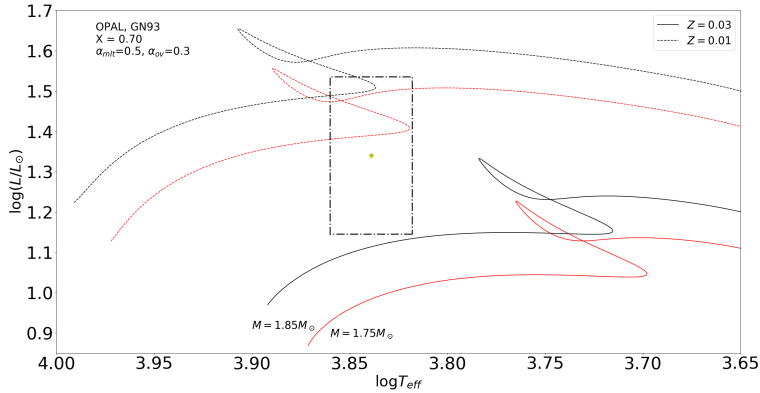


Figure 7.1: Stellar evolution tracks for two different masses with two different metal abundances. Each track has  $X = 0.70$ ,  $\alpha_{mlt} = 0.5$  and  $\alpha_{ov} = 0.3$ . The red lines indicate tracks with masses of  $M = 1.75M_\odot$ , and black lines indicate  $M = 1.85M_\odot$ . The full lines have  $Z = 0.03$  and dashed lines  $Z = 0.01$ . The black dashed box shows the three sigma uncertainties on  $T_{\text{eff}}$  (from Lenz et al. (2010)).

Numerical results for the initial hydrogen abundances can be seen on Fig. 7.2. The line and color convention corresponds to that of Fig. 7.1, with the difference being the line type indicating the values of  $X$  instead. Here it is also clear that the initial hydrogen abundance affects the luminosity (however less than the  $Z$ ). Higher hydrogen abundance causes a smaller helium abundance (when  $Z$  is held constant) HVORFOR ER LUM STØRRE?.

$\alpha_{mlt}$  and  $\alpha_{ov}$  are parameters that are not easily chosen, since they are purely empirical and depend strongly on the prescription used in the modeling (see Sec. 6.1.3. For the  $\alpha_{mlt}$  the standard value in **MESA** is around 1.8. The Warsaw-New Jersey stellar evolution code used to calculate models for 44 Tau by (Lenz et al., 2010) has the same mixing-length prescription as **MESA**. Their results showed that models with mixing length of  $\alpha_{mlt} > 0.2$  gave the best fits, confirming the assumption that smaller mixing lengths than the sun is needed in order to model these stars. However, **MESA** is not computationally capable of handling a mixing length below 0.2 which is not surprising as it would mean that energy transport by convection in the outer layers is almost non existing. This also underlines the fact that convection is treated differently in each stellar evolution code, and parameters such as  $\alpha_{mlt}$  needs to be carefully examined in the grid. It can also be argued that since  $\delta$  Sct stars have a much smaller convection layer than that of the Sun, the convection will not be as efficient. Trampedach & Stein (2011) calculated a range of mixing lengths through a grid simulation of solar type structures. One of the results can be seen on Fig. 7.3.

The mixing length is predicted to be smaller for higher values of  $T_{\text{eff}}$ , as expected. Both 44 Tau and HD 187547 are out of range in  $T_{\text{eff}}$  space, since the

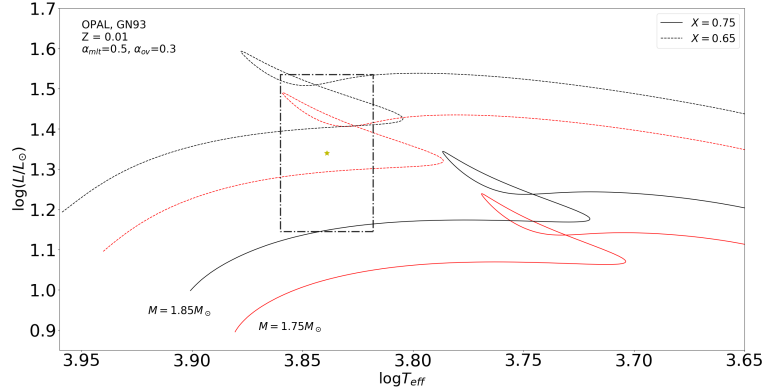


Figure 7.2: Stellar evolution tracks for two different masses with two different metal abundances. Each track has  $Z = 0.01$ ,  $\alpha_{mlt} = 0.5$  and  $\alpha_{ov} = 0.3$ . The red lines indicates tracks with masses of  $M = 1.75M_{\odot}$ , and black lines indicate  $M = 1.85M_{\odot}$ . The full lines have  $X = 0.65$  and dashed lines  $X = 0.75$ . The black dashed box indicates the three sigma uncertainties on  $T_{\text{eff}}$  (from Lenz et al. (2010)).

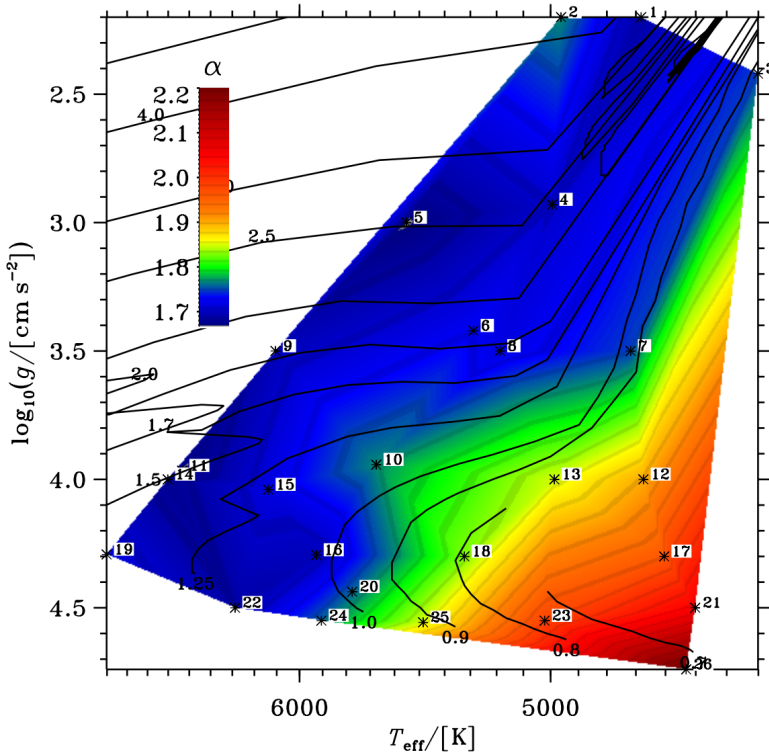


Figure 7.3: Mass mixing lengths in units of pressure scale height  $H_p$  in the  $T_{\text{eff}}$ -  $\log g$  plane. (Trampedach & Stein, 2011).

mixing length range here is calculated based on solar-like structures. However, the trend in mixing length is still applicable to intermediate mass stars. As an initial grid we therefore choose values of  $\alpha_{mlt}$  between 0.2 and 0.8. Analogous to the mixing length, the convective overshoot near the core is described with the convective core overshoot parameter  $\alpha_{ov}$ . As it is typically in the order of 0.1-0.2 (Kippenhahn et al., 1990), we here choose values between 0.1-0.3.

Some models in the grid were not possible to compute with the current equations in MESA. For  $1.5M_\odot$  it was not possible to compute models with a metallicity higher than 0.02, if the initial He abundance is low. For  $1.80M_\odot$  three tracks were excluded as they could not be computed either. The initial grid used here can be seen in Table 7.1.

Table 7.1: Values and step sizes for all parameters in the grid calculated in this work.

	values	stepsize
X	0.65-0.75	0.05
Z	0.01-0.03	0.01
Mass/ $M_\odot$	1.5-2.2	0.05
$\alpha_{mlt}$	0.2-0.8	0.3
$\alpha_{ov}$	0.1-0.3	0.1

Some of these combinations did however not converge properly, and could therefore not be included in the grid. These models are:

- $M = 1.50M_\odot$ : combinations with  $X = 0.75$  and  $Z = 0.02$  or  $Z = 0.03$
- $M = 1.55M_\odot$ : combinations with  $X = 0.75$  and  $Z = 0.03$
- $M = 1.95M_\odot$ : combinations with  $X = 0.75$  and  $Z = 0.03$
- $M = 1.80M_\odot$ : combinations with  $X = 0.75$  and  $Z = 0.02$  and  $\alpha_{mlt} = 0.2$
- $M = 1.90M_\odot$ : combinations with  $X = 0.75$  and  $Z = 0.02$  and  $\alpha_{mlt} = 0.8$

It is unclear why these exact combinations have numerical issues, since it would require an investigation beyond the scope of this work. However, they all have in common that the initial hydrogen abundance is very high at  $X = 0.75$ . This might explain most of the issues since this value is in fact higher than the initial value of the interstellar medium it was born in, which can practically never be true. However, the reason for still including them is that models might still reproduce these high values due to the numerical calculations. So if a model has this value it can be interpreted as an example of the imperfect theory behind the codes.

## 7.2 Resolution and varcontrol

As mentioned previously in Sec. 6.1, they way MESA works is to fulfill calculations in time steps that are non-equidistant. As a result of this, models on a track can be far apart if the evolution is fast. This means that models on the main-sequence are well resolved, while the models on fast stages (particularly post-ms contraction phase) are fare apart in terms of structure. Since every model calculated in MESA yields one model in GYRE, this also results in the frequencies being very different from one model to another, which should be considered when calculating the  $\chi^2$  (see Sec. 7.3). An example can be seen on Fig. 7.4 where, the radial fundamental mode is plotted as a function of timestep. The lower panel of Fig. 7.4 is the same models corresponding to middle panel but where the radial fundamental mode frequency difference between models,  $f_1(i+1) - f_1(i)$ , is plotted as a function of time. This shows that the resolution in the frequency space is as high as 0.18 cyc/day for this track (some tracks go up to 0.2). The highest point is, however, in the very beginning of the main sequence, and not on the post-main sequence contraction phase, where it is favorable to have a high resolution.

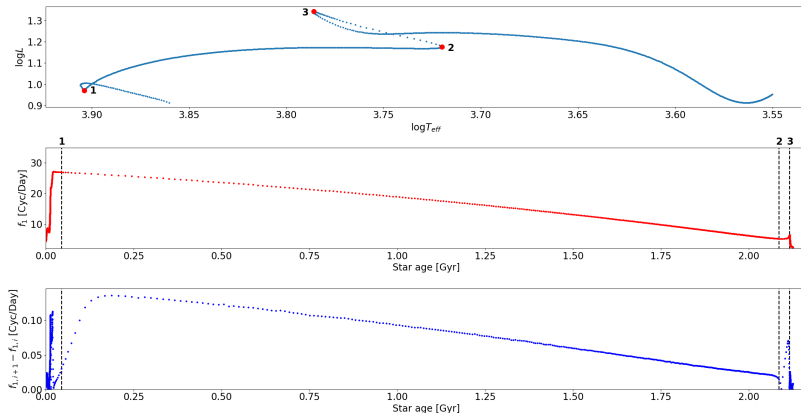


Figure 7.4: Resolution at different stages of an evolution of a track with  $M=1.85M_{\odot}$ ,  $X=0.75$ ,  $Z=0.02$ ,  $\alpha_{mlt}=0.5$ ,  $\alpha_{ov}=0.3$ . The begininng of the main sequence is marked with a bold "1", continuing until "2" where the post-main sequence contraction phase starts. At "3" all hydrogen has been exhausted in the core, and the star is in the post-main sequence expansion phase. Middle panel: Here the fundamental frequency is plotted as a function of time. The dashed lines indicate the stages corresponding to those in the middle panel. Lower panel: Shows the absolute difference in fundamental frequency between two subsequent models.

Since 44 Tau has earlier been identified to be in the post-ms contraction phase (and since we cannot exclude that possibility for Superstar either) the resolution of the models in MESA needs to be adjusted to allow for a higher chance of finding a good fit. It is possible to simply force smaller timesteps,

but this is not ideal since it would not only increase the computation time on the fast evolutionary stages, but the entire track. Since a better resolution is not really needed on the ms, it is therefore better consider an alternative parameter that does not waste computation in areas where it is not needed.

There are more than one way of doing so. It is possible to set a limit for magnitude of max change in temperature and photosphere with the `delta_lgTeff_limit`, or alter the minimum and maximum number of grid points in a model with `mesh_delta_coeff` (a higher values decreases number). These parameters need to increase the resolution in the right area, but also within a resonable amount of computation time. The parameter found to be most efficient in this project is the `varcontrol_target` parameter. This parameter is assigned a value describing the relative variation in the structure from one model to the next. The timestep then adjust accordingly, depending if the variation is smaller or larger than the value. Increasing the resolution through this value does also increase the computation time, however, reasonably. An example of this can be seen on Fig. 7.5 where the same track is plotted with different values of `varcontrol_target`. It is here found that a value of 5e-5 is sufficient in making the resolution satisfactory for this work.

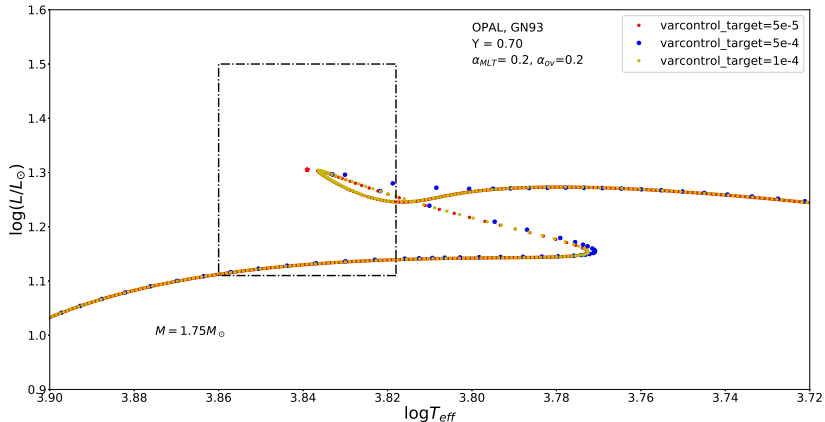


Figure 7.5: Evolution of three tracks with same initial parameters, but different values of `varcontrol_target` where 1d-4 is default in `MESA`. It can be seen that the resolution drops significantly for the value 5d-4. Therefore, a slightly smaller value of 5d-5 is chosen for this work.

Some tracks are still better resolved than others. A general tendency from the computed tracks are that models with overshoot below 0.2 are not resolved nearly as well as models with high overshoot of 0.3, which can also be seen on Fig. 7.6. Particularly the Henyey hook cannot be reproduced very well for overshoot of 0.1. The details as to why this occurs is beyond the scope of this work, however it is very important to take into consideration when evaluating results as tracks with low overshoot will automatically have fewer models and therefore limited chances of fitting well to observations.

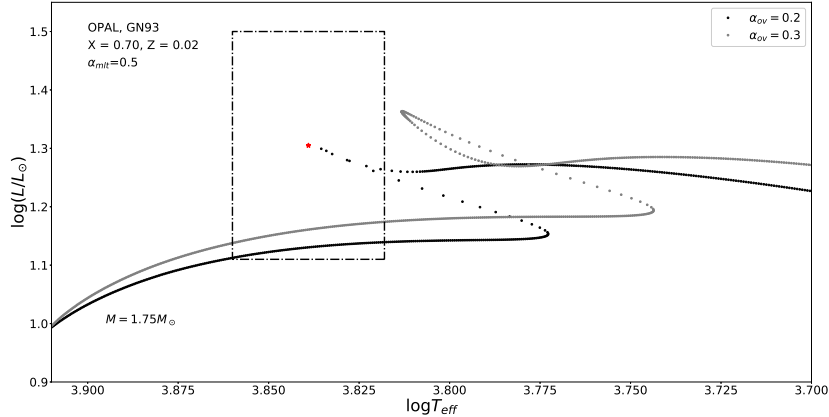


Figure 7.6: Two models of the same track, but with different overshoot.

## 7.3 chi2 testing

### 7.3.1 Finding the best model

In order to find out how well/fitted a model is, a comparison with stellar parameters is needed. By just comparing models to luminosity, effective temperature and surface gravity, it is difficult to find an estimate on the evolutionary stage as the best model on one track might be on the main sequence, whereas the best model on a different track is on the post-main sequence. Therefore, frequencies are need as additional observational parameters for comparison (as they, as discussed in Sec. 4, change with evolution). There is more than one way of doing the comparisons, but in this work a  $\chi^2$  test is used.  $\chi^2$  yields a value for each models, allowing us to find models with lowest  $\chi^2$  values. The Pearson's goodness of fit test is commonly written as

$$\chi_j^2 = \sum_{i=1}^I \left( \frac{\nu_{i,j}^{theo} - \nu_i^{obs}}{\sigma_i} \right)^2, \quad (7.1)$$

where  $\nu_i^{obs}$  is the observed parameter for model i,  $\nu_i^{theo}$  is the corresponding theoretical parameter and  $\sigma_i$  is the uncertainty for the parameter. It provides a number that somewhat describes how close the fitting parameters are tp the corresponding observed parameters. However, there is more than one way of doing a  $\chi^2$  test, as its implementation depends on the work, and particularly the goal that is desired. There are a few assumption that needs to be taken into consideration before implementing a  $\chi^2$  test. Most importantly, statistically speaking, a  $\chi^2$  test does not provide any information on how well individual parameters fit, or how likely a model is to be good. As the goal of this project is to find the most likely evolutionary stage, the  $\chi^2$  values can simply be used as a way of *comparing* between the different models. So models with the lowest  $\chi^2$  are the models with parameters closest to the observed parameters.

These thereby provide an age span and a likely evolutionary stage. If the  $\chi^2$  values are to be compared between the different models, then they need to be calculated under the same conditions. This means that calculations should be done with the same number of fitting parameters for all models (since they otherwise are not comparable). For instance, if one model have more fitted frequencies than another, the  $\chi^2$  with the model with more fitting parameters will have an extra link, causing it to naturally be larger than the  $\chi^2$  for the model with fewer fitted frequencies, making their  $\chi^2$  incomparable.

### 7.3.2 44 Tau

#### 7.3.2.1 l=0 modes

For 44 Tau, the frequencies of the fundamental mode and first overtone are well-determined. These frequencies act as a constraint for the  $l=0$  mode models. Initially the  $l=0$  modes are computed using GYRE for the entire grid described in Sec. 7.1. Here, we have an initial constraint from only the frequencies corresponding to the radial fundamental mode and first overtone and the global parameters. The  $\chi^2$  for this initial run then becomes

$$\chi_j^2 = \left( \frac{\nu_{\text{fund,obs}} - \nu_{j}^{\text{fund,theo}}}{\sigma_{\text{fund},j}} \right)^2 + \left( \frac{\nu_{\text{first,obs}} - \nu_{j}^{\text{first,theo}}}{\sigma_{\text{first},j}} \right)^2 + \left( \frac{T_{\text{eff}}^{\text{obs}} - T_{\text{eff},j}^{\text{theo}}}{\sigma_{T_{\text{eff}},j}} \right)^2 \quad (7.2)$$

$$+ \left( \frac{\log g^{\text{obs}} - \log g_j^{\text{theo}}}{\sigma_{\log g,j}} \right)^2 + \left( \frac{\log L^{\text{obs}} - \log L_j^{\text{theo}}}{\sigma_{\log L,j}} \right)^2, \quad (7.3)$$

where  $\chi_j^2$  is the  $\chi^2$  for the  $j$ 'th model. For  $T_{\text{eff}}$ ,  $\log g$  and  $\log L$  the  $\sigma$  used is simply the uncertainties from observations. Notice here that even though the frequencies are calculated for the entire track, the  $\chi^2$  is not calculated for models on the pre-main sequence.

For the frequencies the  $\sigma$  is naturally very small (in the order of  $10^{-6}$ Cyc/day), since the uncertainty on observations depend only on the observation time. Long observation times of 44 Tau therefore results in very narrow peaks. It is very nice to know a parameter to this precision, but as shown in Eq. 7.3 a small uncertainty will result in high values of  $\chi^2$ . This is not a problem on its own, as the  $\chi^2$  only represent how well the model fits observation. If this value is extremely high it does not necessarily mean that the models are not good models for the star, but that a model precision is simply not comparable to frequency precision. In other words, no model will ever get close to fitting well. Also, by only dividing by the uncertainties the resolution of the track is not taken into consideration. As shown in Sec. 7.2 the resolution of the track is important as fewer models in one area decreases the possibility of having a good fit. This also means that a model frequency can change a lot between two time steps if the resolution is low, and this should be taken into account. In

this work the following is prescription is therefore applied to the frequencies:

$$\chi^2 = \frac{1}{\alpha} \sum_{i=1}^I \frac{(v_i^{\text{obs}} - v_{i,j}^{\text{theo}})^2}{(\sigma_i^{\text{obs}})^2 f_i(\Delta\nu_{i,j})} \quad (7.4)$$

where  $i$  in this case is the different frequencies (i.e  $I=2$  for  $l=0$  calculations where we only compare to fundamental frequency and first overtone),  $j$  is the  $j$ 'th model, and  $\alpha$  is a scaling parameter.  $f_i(\Delta\nu_{i,j})$  is a function that artificially increases the sigmas on the frequencies

$$f_i(\Delta\nu_{i,j}) = \frac{\nu_j - \nu_{j-1}}{\sigma_{\text{obs},i}}, \quad (7.5)$$

where the distance in frequency space is taken into consideration for the  $j$ 'th model. Smaller distances in the frequency space between model means a higher  $f_i(\Delta\nu_{i,j})$ , hence, as smaller  $\chi^2$ . Runs both with and without the uncertainty pump will be made to test the difference in the main result.

As of yet only  $l=0$  modes have been fitted. Calculating corresponding  $l=1$  and  $l=2$  modes for all models is time consuming, and therefore a selection criteria is needed. This is done by first finding the model with the lowest  $\chi^2$  is for each track. From all of these the best 5% are found for both methods, respectively. These models and their initial parameters are shown in Table 7.2 and Table 7.3.

It is possible that the 5% best models from the overall grid (and not by first selecting the best from each track) might more than one model on each tracks that are in the 5% range. But by first selecting the model with the lowest  $\chi^2$  value for each track, a wide range of parameter combinations is ensured. It forces an estimate on the evolutionary stage at all areas of the grid, including the very outskirts. The disadvantage of this is that it makes it more difficult to identify a more possible parameter combination, since there cannot be more than one model in the 5% range on a track. However, as the end goal is to find an estimated evolutionary stage and a single best model, the method is adequate.

One thing that could cause a the best model to be shifted towards a different parameter combination is if the grid. Since  $\chi^2$  only provide a value to compare to other models, it does not give an indication of how likely a parameter space is. This also means that the  $\chi^2$  for the frequency space can deviate a lot from the  $\chi^2$  from the other observable parameters. To ensure that the 5% models are also within the observable parameter space of  $\log g$  and  $T_{\text{eff}}$ , a scatter plot is made which can be seen on Fig. 7.7.

Here,  $\log g$  is plotted as a function of  $T_{\text{eff}}$  and color coded with the corresponding  $\chi^2$ . The  $1\sigma$  uncertainty on  $\log g$  and  $T_{\text{eff}}$  is marked with a black stippled line. Some of the scatter plots shows expected tendencies such as  $l$ ,  $\log g$ ,  $T_{\text{eff}}$  and profile numbers. Since higher profile number is at a later stage<sup>1</sup>,

---

<sup>1</sup>Note that the profile number does only indicate the stage of that individual track i.e profile number 900 on one tracks is not necessarily at the same stage for the same profile number on a different track.

Table 7.2: hest

Model	X	Z	Y	$M[M_\odot]$	$\alpha_{mlt}$	$\alpha_{ov}$	$\log T_{\text{eff}}$	$\log L$	$\log g$	$\chi^2(\text{method1})$
-------	---	---	---	--------------	----------------	---------------	-----------------------	----------	----------	--------------------------

the effective temperature is much lower for lower profile numbers. There is a gap in models around  $T_{\text{eff}} = 3.79$  in the 5% selection criteria. From the profile number it is also clear that the models distributes into two groups where the lower profile numbers corresponds to those on the pre-ms and the higher profile numbers are ms and thereafter. The pre-ms models will be ignored since they are not as reliable as the rest of the models. This group of models is also significantly further away from the errorbox and they will therefore not affect the main result.

The lowest  $\chi^2$  linearly seems to linearly decrease with  $T_{\text{eff}}$ . This is because  $\log g$  is strongly related to  $\rho$  (hence,  $\Delta\nu$  and  $T_{\text{eff}}$ ). For the element abundances, there is a trend a that lower values of  $\log g$  yield lower values of Z and X, in particular. This falls out of Eq. ?? as high abundances of hydrogen and/or metallicity causes a lower mean molecular weight. Since  $\mu \propto \rho \propto g$ , a smaller

Table 7.3: skinke

Model	X	Z	$M[M_\odot]$	$\alpha_{mlt}$	$\alpha_{ov}$	$\log T_{\text{eff}}$	$\log L$	$\log g$	$\chi^2$	$\chi^2_{pum}$
1356	1.50	0.65	0.01	0.2	0.1					
1247	1.50	0.65	0.01	0.5	0.1					
1218	1.50	0.65	0.01	0.8	0.1					
1443	1.55	0.70	0.01	0.2	0.3					
1297	1.55	0.70	0.01	0.5	0.3					
1257	1.55	0.70	0.01	0.8	0.3					

---

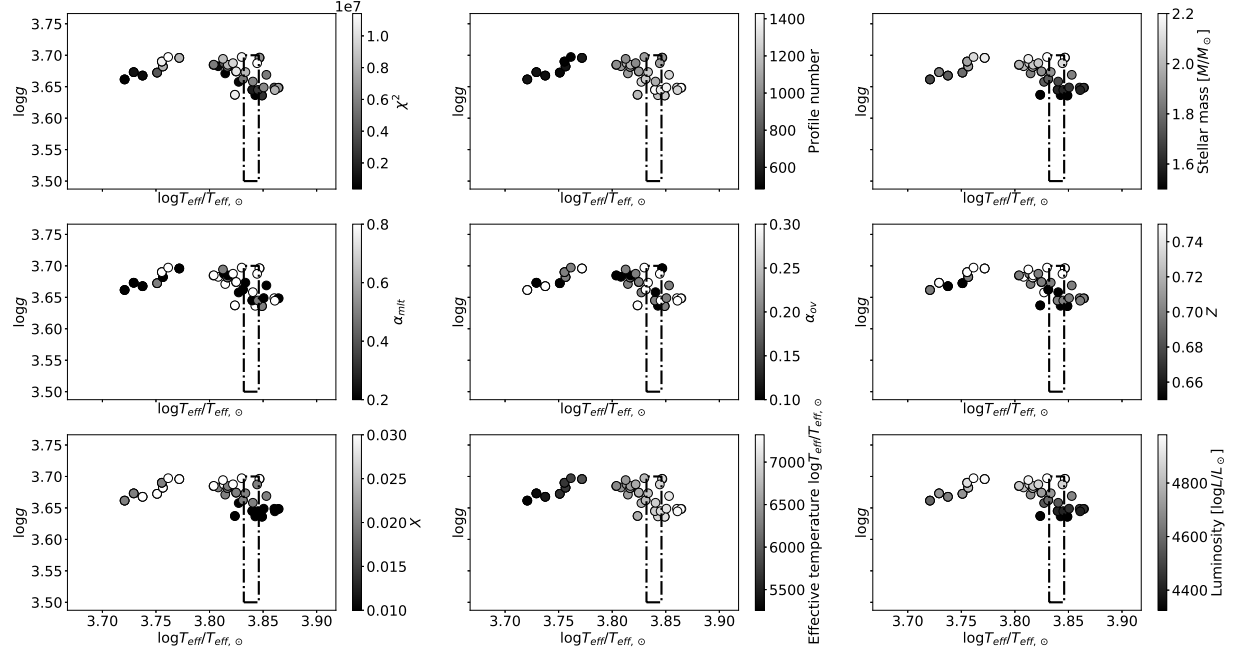


Figure 7.7: Scatter plots showing  $T_{\text{eff}}$ ,  $\log g$  color coded with nine different parameters for the 5% best models (without resolution control). The plots color coded with  $T_{\text{eff}}$  and  $\log g$  are plotted to show that the plotting method works correctly. The run was made with the Lenz observational parameters set.

value of X or Z yields a smaller value for g as well. Since g is also directly proportional to the mass, the mass decreases with  $\log g$  in the plot as well.

There seems to be no recognizable trend in the  $\alpha_{\text{mlt}}$  and  $\alpha_{\text{ov}}$  color coding. Since there is a definite correlation between the convection and structure of the star, it would be expected to see a trend between the mixing length or overshoot parameter and  $\log g$  and  $T_{\text{eff}}$ . Since this sample is small, it cannot be excluded that there is a trend that can be found if mode data points were included.

### 7.3.2.2 l=0,1,2 modes

A new calculation was conducted in GYRE for  $l=0$ ,  $l=1$  and  $l=2$  modes for all of these models. The frequencies produced gives a further constrain of the best models as all frequencies can now be compared with observations. Since mode identification is not complete for 44 Tau the radial  $n,l,m$  for the frequencies are not finally determined. Therefore they cannot be compared to the individual frequencies calculated in the model without first giving an estimated guess on the  $n,l$  and  $m$ . Therefore a calculation is conducted based on the fact that  $n,l$  and  $m$  is known for the models. To ensure that the  $\chi^2$  are comparable between each model, as mentioned earlier, the models all need to have the same amount of fitting parameters. This is not an issue in the first  $\chi^2$  calculations

with  $l=0$ , since the initial  $\chi^2$  is only based on the same two frequencies for all models. But for  $l=1$  and  $l=2$  the picture is less simple as the number of fitting parameters may vary from model to model, unless it is taken into consideration. The first way to do so is to weight each frequency individually and take the likelihood into account. Though this method probably provides a more detailed and statistically stringent result, it does require a very thorough estimate and evaluation of the single frequencies. This is beyond the scope of this work, and instead it is therefore made sure in the way the code is constructed, that this can only be an issue if the number of theoretically produced frequencies is lower than the observed number 8 and this is unlikely to happen as these models have already been sorted out in the first  $\chi^2$  round.

It is carried out in the following way: for each model, each individual model-frequency is compared to all observed frequencies and the best match (i.e. the smallest difference) is thereby assumed to be the closest frequency. This is repeated from the lowest to highest frequency until all model-frequencies have been given a best match observation frequency. This means that the observed frequency will be given the  $n.l$  and  $m$  of the best -matching model-frequency. Each model then has an estimated set of frequencies where  $\chi^2$  can be computed. This of course does not take into consideration that some frequencies have an estimated radial order and spherical degree. Nor does it take into consideration that the radial fundamental mode and first overtone are already determined (and might match it to  $n$  that are higher, however these models should be excluded as their match will not be good if the two first frequencies do not match expectations). This yields a  $\chi^2$

$$\chi^2 = \left( \frac{\nu_{\text{all,obs}}^i - \nu_{\text{all,theo}}^i}{\sigma_{\text{first}}^i} \right)^2 + \left( \frac{T_{\text{eff,obs}}^i - T_{\text{eff,theo}}^i}{\sigma_{T_{\text{eff}}}^i} \right)^2 + \left( \frac{\log g_{\text{obs}}^i - \log g_{\text{theo}}^i}{\sigma_{\log g}^i} \right)^2 + \left( \frac{\log L_{\text{obs}}^i - \log L_{\text{theo}}^i}{\sigma_{\log L}^i} \right)^2, \quad (7.6)$$

From these, the models with the lowest  $\chi^2$  is found for the two different luminosities respectively. .

### 7.3.3 Results

The best models found for different runs of 44 Tau are shown in Table 7.6. It can here be seen that the variation from GAIA run and Lenz run does not affect the total result. It does however shift the best found model if only including the observational parameters. The reason for this is that the frequencies weigh more in the  $\chi^2$  than the observational parameters. Artificially enhancing the uncertainties on the frequencies does shift the best model, but the total  $\chi^2$  is ...WORSE/BETTER?.

The best model results for the Lenz parameter run can be seen on Fig. 7.8. The hrd shows the tracks for masses  $M = 1.5, 1.6, 1.7, 1.8, 1.9, 2.0, 2.0$  with the combination of  $X = Z = \alpha_{mlt}, \alpha_{ov}$ . The best total model is marked with a cyan blue dot, on the track marked with red. The green points shows the best

profile number	M[ $M_{\odot}$ ]	X	Z	$\alpha_{mlt}$	$\alpha_{ov}$	$\backslash$ teff	$\backslash$ logg	$\backslash$ l	$\chi_{tot}$	$\chi_{obs\_params}$	$\chi_{freqs}$	o
----------------	------------------	---	---	----------------	---------------	-------------------	-------------------	----------------	--------------	----------------------	----------------	---

Table 7.4: text

5% models if the criteria is the total  $\chi^2$ <sup>22</sup>. Blue dots are the 5% best models if only observational parameters  $\log g$ ,  $T_{\text{eff}}$ ,  $l$  is included in the  $\chi^2$ , whereas the red dots is the 5% if the  $\chi^2$  is only calculated from the frequency fits. The green tracks shows the best track with the black dot marking the best model if the frequency uncertainties have been artificially enhanced as in Eq. 7.4. This track has the parameter combination of  $M = 1.5, 1.6, 1.7, 1.8, 1.9, 2.0, 2.0$  with the combination of  $X = Z = \alpha_{mlt}, \alpha_{ov}$ .

The green points tend to overlap the red points, which indicates that the frequencies are highly more weighted than the observational parameters. The frequencies thereby controls the final outcome, explaining why there is no difference in the main result by changing between GAIA or Lenz observations. The best 5% models from frequencies seems to be divided into two groups whereas the group near lower temperatures are models on the pre-ms. Since the pre-ms models were loaded from pre-calculated models as discussed in Chap. 6, causing different relaxation of the models, the pre-ms and particularly the frequencies on the pre-ms should not be trusted. Since the best model is between the other group it does not make a difference for the main result, but if further tests should be done with the 5%, they should be excluded from the sample.

The best model is placing 44 Tau on the post-ms shortly after hydrogen exhaustion in the core. It is not within the three-sigma errorbars from the observations (whereas the best model with artificially pumped frequencies is), which is also clear since there are other models that are closer to the observed parameters. However, since the frequencies weigh much more, the overall  $\chi^2$  is lower. The frequency fit can be seen on Fig. 7.9. Here, the observational frequencies are plotted with dimensionless power on the y-axis. They color-coded are color-coded by the spherical degree as follows:  $l = 0$  are red,  $l = 1$  are blue and  $l = 2$  are green, with dimensionless powers of 1,2 and 3. The black lines indicate the matched theoretical frequency, and the gray lines at the bottom represents all theoretically produced frequencies. The naming of the frequencies are defined as in Table ???. Stippled lines are lines of uncertainty on the frequencies, although these are so small that they are not visible. Since the uncertainty is so small, technically none of the theoretical frequencies are matched within the uncertainties. However, they are all matched within a range of  $0.2d^{-1}$ . The red named text are two modes for which mode identification differs from the theoretically predicted with the  $\chi^2$  fitting code for the frequencies. This is for  $f_{10}$  and  $f_2$  where the estimated modes from mode identification is  $l = 2$  and  $l = 1$ , whereas they were here estimated to be  $l = 1$  and  $l = 2$ , respectively. This could be due to different reasons: 1) The pulsation code does not calculate the theoretically produced frequencies correctly. At this point it is already a well-known issue that the theory behind these type of oscillations does not comply well with observations. Lenz et al. (2010) was indeed successfull with modeling 44 Tau, but this example is the first one of its kind where all modes where reproduced theoretically. More often, pulsation codes does not match observations. 2)

---

<sup>22</sup>The total  $\chi^2$  is the  $\chi^2$  from all frequencies, including  $l = 1$  and  $l = 2$  modes plus the  $\chi^2$  from observational parameters.

The  $\chi^2$  routine used in this project does not match the frequencies correctly, resulting in the spherical degrees to be found incorrectly. As discussed earlier in this chapter, the routine only considers the best match frequency, and does not take spherical degree into account at any point. It only guesses it based on the theoretically produced ones. 3) Due to the high uncertainty in mode identification, some of the modes have been done incorrectly. This is the more likely scenario since 1) and 2) would probably cause issues for more than two modes, and would not have been able to fit the rest either. There is also strong evidence that some modes could be identified wrongly due to the model dependency of the mode identification. It can be seen on Fig. ?? that the choice of mixing length affects the mode identification significantly. EXPLAIN FIGURE. These models are based on frozen convection where the mixing length describes the local convection. However, time-dependent convection is needed in order to describe the full picture of convection, and the difference in mode identification is significant (Dupret et al., 2005), (Victoria Antoci 2019, private communication).

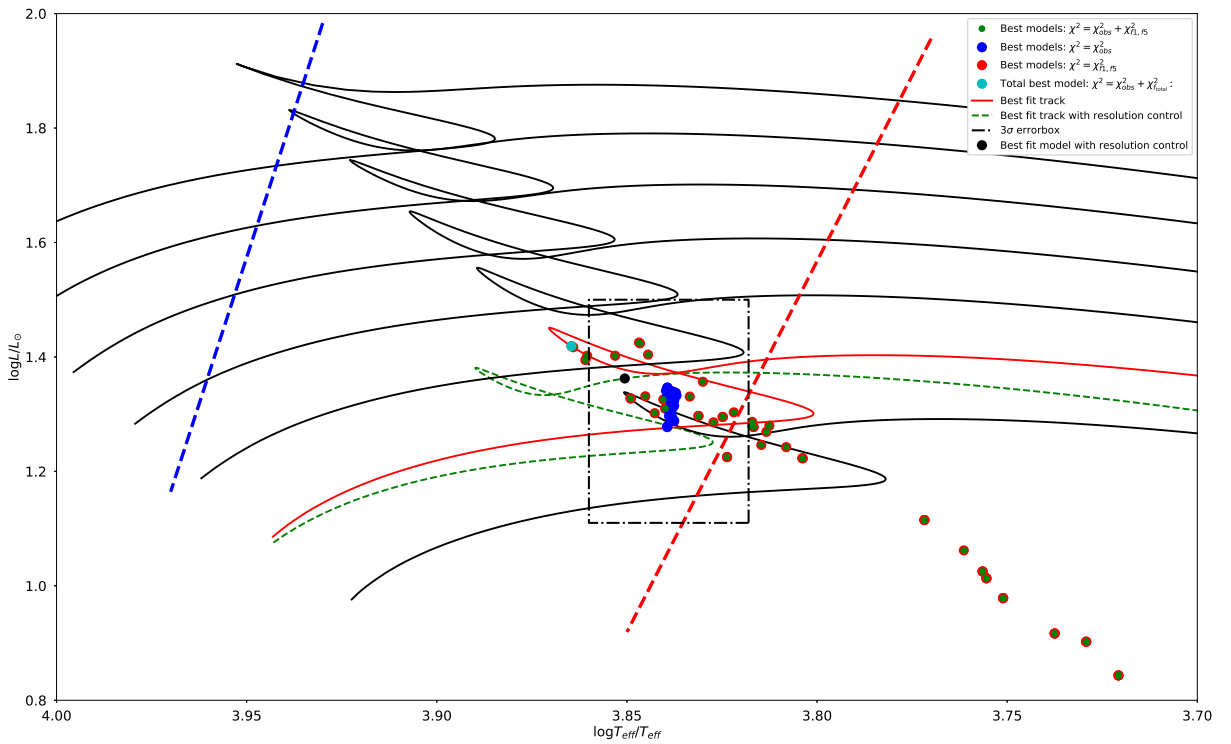


Figure 7.8

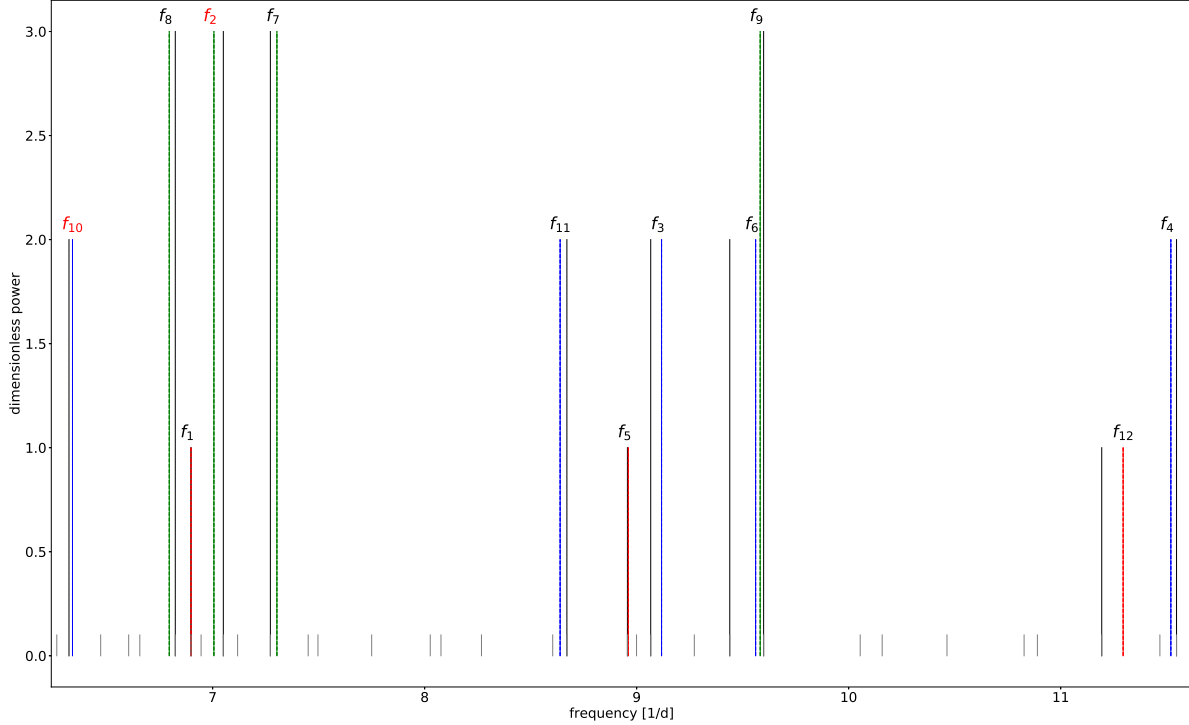


Figure 7.9

## 7.4 Superstar

On the contrary to 44 Tau, no modes are well enough determined to use an initial constraint for the models of this star. Instead of fitting the frequencies it is therefore more favourable to fit the large frequency separation, introduced in Sec. 4. This can be calculated as

$$\Delta\nu = \nu_{n+1} - \nu_n, \quad (7.7)$$

the frequency difference between two ( $l=0$ ). The  $\chi^2$  can now be calculated using the observed large frequency separation of 3.5 cycles per day (Antoci et al., 2014), calculated the same way as Eq. 7.4, with method one Eq. 7.4. Employing the standard deviation as Eq. ?? cannot be done the same way as for 44 Tau since there is only one parameter to sum over. Therefore, the 5% models with the smallest  $\chi^2$  are found only through the first method, and results are shown in Table 7.5.

For modes higher than  $l=0$ , calculating the  $\chi^2$  for Superstar is significantly more complicated for Superstar, since it is based on the large frequency separation. When  $l$  becomes larger than zero, the frequency separation depends significantly on the mixed modes and radial order. Therefore, this part is beyond the scope of this work.

Table 7.5: hest

Model	X	Z	Y	$M[M_\odot]$	$\alpha_{mlt}$	$\alpha_{ov}$	$\log T_{\text{eff}}$	$\log L$	$\log g$	$\chi^2$
-------	---	---	---	--------------	----------------	---------------	-----------------------	----------	----------	----------

#### 7.4.1 Results

The best models found for different runs of 44 Tau are shown in Table 7.6. It can here be seen that the variation from GAIA run and Lenz run does not affect the total result. It does however shift the best found model if only including the observational parameters. The reason for this is that the frequencies weigh more in the  $\chi^2$  than the observational parameters. Artificially enhancing the uncertainties on the frequencies does shift the best model, but the total  $\chi^2$  is ...WORSE/BETTER?.

The best model results for the Lenz parameter run can be seen on Fig. 7.8. The hrd shows the tracks for masses  $M = 1.5, 1.6, 1.7, 1.8, 1.9, 2.0, 2.0$  with the combination of  $X = Z =, \alpha_{mlt}, \alpha_{ov}$ . The best total model is marked with a cyan blue dot, on the track marked with red. The green points shows the best 5% models if the criteria is the total  $\chi^2$ <sup>23</sup>. Blue dots are the 5% best models if

---

<sup>23</sup>The total  $\chi^2$  is the  $\chi^2$  from all frequencies, including  $l = 1$  and  $l = 2$  modes plus the  $\chi^2$  from observational parameters.

profile number	M[ $M_{\odot}$ ]	X	Z	$\alpha_{mlt}$	$\alpha_{ov}$	$\log g$	$\log g$	$\chi_{tot}$	$\chi_{obs\_params}$	$\chi_{freqs}$	observation
----------------	------------------	---	---	----------------	---------------	----------	----------	--------------	----------------------	----------------	-------------

Table 7.6: text

only observational parameters  $\log g$ ,  $T_{\text{eff}}$ ,  $\xi$  is included in the  $\chi^2$ , whereas the red dots is the 5% if the  $\chi^2$  is only calculated from the frequency fits. The green tracks shows the best track with the black dot marking the best model if the frequency uncertainties have been artificially enhanced as in Eq. 7.4. This track has the parameter combination of  $M = 1.5, 1.6, 1.7, 1.8, 1.9, 2.0, 2.0$  with the combination of  $X = Z = \alpha_{mlt}, \alpha_{ov}$ .

The green points tend to overlap the red points, which indicates that the frequencies are highly more weighted than the observational parameters. The frequencies thereby controls the final outcome, explaining why there is no difference in the main result by changing between GAIA or Lenz observations. The best 5% models from frequencies seems to be divided into two groups whereas the group near lower temperatures are models on the pre-ms. Since the pre-ms models were loaded from pre-calculated models as discussed in Chap. 6, causing different relaxation of the models, the pre-ms and particularly the frequencies on the pre-ms should not be trusted. Since the best model is between the other group it does not make a difference for the main result, but if further tests should be done with the 5%, they should be excluded from the sample.

The best model is placing 44 Tau on the post-ms shortly after hydrogen exhaustion in the core. It is not within the three-sigma errorbars from the observations (whereas the best model with artificially pumped frequencies is), which is also clear since there are other models that are closer to the observed parameters. However, since the frequencies weigh much more, the overall  $\chi^2$  is lower. The frequency fit can be seen on Fig. 7.9. Here, the observational frequencies are plotted with dimensionless power on the y-axis. They color-coded are color-coded by the spherical degree as follows:  $l = 0$  are red,  $l = 1$  are blue and  $l = 2$  are green, with dimensionless powers of 1, 2 and 3. The black lines indicate the matched theoretical frequency, and the gray lines at the bottom represents all theoretically produced frequencies. The naming of the frequencies are defined as in Table ???. Stippled lines are lines of uncertainty on the frequencies, although these are so small that they are not visible. Since the uncertainty is so small, technically none of the theoretical frequencies are matched within the uncertainties. However, they are all matched within a range of  $0.2d^{-1}$ . The red named text are two modes for which mode identification differs from the theoretically predicted with the  $\chi^2$  fitting code for the frequencies. This is for  $f_{10}$  and  $f_2$  where the estimated modes from mode identification is  $l = 2$  and  $l = 1$ , whereas they were here estimated to be  $l = 1$  and  $l = 2$ , respectively. This could be due to different reasons: 1) The pulsation code does not calculate the theoretically produced frequencies correctly. At this point it is already a well-known issue that the theory behind these type of oscillations does not comply well with observations. Lenz et al. (2010) was indeed successfull with modeling 44 Tau, but this example is the first one of its kind where all modes where reproduced theoretically. More often, pulsation codes does not match observations. 2) The  $\chi^2$  routine used in this project does not match the frequencies correctly, resulting in the spherical degrees to be found incorrectly. As discussed earlier in this chapter, the routine only considers the best match frequency, and does

not take spherical degree into account at any point. It only guesses it based on the theoretically produced ones. 3) Due to the high uncertainty in mode identification, some of the modes have been done incorrectly. This is the more likely scenario since 1) and 2) would probably cause issues for more than two modes, and would not have been able to fit the rest either. There is also strong evidence that some modes could be identified wrongly due to the model dependency of the mode identification. It can be seen on Fig. ?? that the choice of mixing length affects the mode identification significantly. EXPLAIN FIGURE. These models are based on frozen convection where the mixing length describes the local convection. However, time-dependent convection is needed in order to describe the full picture of convection, and the difference in mode identification is significant (Dupret et al., 2005), (Victoria Antoci 2019, private communication).



# 8 Discussion and future work

In this chapter the results will be discussed in more detail for the purpose of proposing any issues and aspects that need to be addressed in future work for obtaining further knowledge and improvement.

Discussion points, and future stuff:

- Testing opacities and element abundances
- Rotation in models (both mesa and GYRE)
- Further analysis of mlt and overshoot in particular - different prescriptions
  - a few models could simply not be converted
  - a more thorough analysis on the grid and which models work
- Additional varcontrol!
- non-adiabatic treatment and excited frequency range
- further mass analysis with petersen diagrams

## 8.1 Grid considerations

The grid of tracks constructed for this project proves sufficient for providing an estimate on the range in the evolutionary stage for 44 Tau and HD 187547. It stretches from a mass of 1.5 to  $2.2 M_{\odot}$  to cover up most of the instability strip in the parameters space. However, as  $\delta$  Sct pulsators have been observed even outside of the instability strip, it is important to include that possibility of more extreme parameter space possibilities. Therefore, further analysis in the future should include a more detailed evaluation of the outer grid bounds to analyse the probability of the best fit models in those ranges. As the mass boundary for  $\kappa$  mechanism is still an ongoing discussion (reference), a larger grid including masses up to  $2.5 M_{\odot}$  should be included in the grid to ensure full coverage. Since  $\alpha_{mlt}$  is a purely empirical parameter and therefore not directly applicable in analytical solutions, there are not many guidelines as how to the range in the grid should be chosen. Here, smaller values were initially chosen due to two reasons: Firstly, the values for  $\alpha_{mlt}$  in (Lenz et al., 2010) is as low as  $\alpha_{mlt} = 0$ . Hence, the values in this project must be correspondingly small in order to compare results more easily. However, this argument becomes faulty as soon as the implementations of  $\alpha_{mlt}$  is not the same in both stellar structure and evolution codes, meaning that the same number has different interpretations. Although, secondly, one might still argue that such small values still is a good estimate for stars with very small convective envelopes, since the convection is not efficient. This is very much still up to discussion, since convective efficiency and how

it affects the excited frequencies, despite efforts (references), still lacks understanding. For this project, the effects of different mixing lenght throughout the HRD is shown on Fig. 6.1, and as earlier discussed in Sec. 6 it primarily has affects the star in the late stage of the subgiant phase. However, the effects it will have on the frequencies is more vast, as can be seen on ...

From this it is clear that the structure changes that follows from different choice of mixing lengths affects the frequencies quite vastly, pushing them to (higher or lower) which could result in a bias in the best 5%, pushing the best model results towards (lower, higher values of  $\log g$ ?). For future work, it would therefore be worthwhile to extend the  $\alpha_{mlt}$  to values as high as the standard solar value of 1.8 in **MESA**. This ensures the exclusion of unconscious bias from the grid choice.

As mentioned in Sec. 7.3.2, the uncertainties of the frequencies are very small, causing the values of the total  $\chi^2$  is completely controlled by the frequencies. A method taking the resolution into consideration was implemented through Eq. 7.5. It was also showed that this made no significant difference to the best 5%, as the  $\chi^2$  values for the frequencies is still significantly higher than for the rest of the parameters. This proves that the resolution is not troublesome enough to cause a change of the best model. (is it though?). It can also be argued that frequencies should naturally be weighed higher as the observations have smaller uncertainties, and that the  $\log g$ ,  $T_{\text{eff}}$ , and  $\log L/L_{\odot}$  should be given correspondingly smaller weights due to higher uncertainties (and disagreements between spectroscopic and photometric values). This is also done automatically in this project since the  $\chi^2$  is calculated by dividing with the uncertainties. However, this does cause the frequencies to weigh much more than intended, and it would therefore be relevant to conduct an implementation of more thoroughly selected weights for all the fitting parameters. (How would this be doe though?).

Even though implementing the resolution into the  $\chi^2$  does not change the main results, it is still favorable to have as many points on a track as time allows. As discussed, this is time consuming computationally, but ensures a minimized  $\chi^2$ . The **target** command in **MESA** allowed for a somewhat better resolution (particularly for tracks with high  $\alpha_{ov}$ ), but more options to increase the resolution even further should be considered in future work. This analysis was primarily focused on the evolutionary stage of the stars, but also depends strongly on the input parameters for the tracks. In this work, the step size of the tracks is bigger than that of Lenz et al. (2010), resulting in a larger difference in parameter space. Thus, models in between these tracks are not considered. Since creating an entire grid is time consuming, doubling it up would take very long, and could prove excessive particularly in those areas of the HRD where it would be less likely to find  $\delta$  Sct pulsations. Instead, grid with smaller step sizes could be constructed around the tracks of either the best 5% models, or those with higher likelihood. The latter is, however,

a different statistical approach where each model input parameter gives a likelihood. Both ways would also allow for a more detailed evaluation of the individual model parameters, particularly the  $\alpha_{mlt}$  and  $\alpha_{ov}$ . By further constructing a narrow but dense grid around the best model, it can be tested if the minimal  $\chi^2$  is still on the original track, or if  $\chi^2$  can be optimized even further.

Throughout this project, the grid constructed was only calculated using gs98 element abundances and OPAL opacities. This was done due to limited time. However, as Lenz et al. (2010) showed in his asteroseismic modeling of 44 Tau, the tracks and thereby the evolutionary stage are affected by this choice. Therefore, a further analysis of the choice is needed in order to determine if the best model  $\chi^2$

## 8.2 Stringent statistics

From a statistical point of view, the  $\chi^2$  test carried out in this work is crudely simplified for the purpose of answering the question of which evolutionary stages the stars are in. The  $\chi^2$  is merely a number that gives the sum of differences for the parameters, but a small  $\chi^2$  does not necessarily mean that that model has the highest **likelihood**. In order to compare  $\chi^2$  between all models in the grid, strictly speaking, the conditions should not change between the models as the individual parameters are then weighted differently. Therefore, since Eq. 7.4 and Eq. ?? are not weighted the same way as the rest of the parameters, the sum of parameters depends on two different weighting methods (even though the  $\alpha$  does somewhat act as a translation between them). This is not a problem in itself, but it is more statistically correct to calculate  $\chi^2$  independantly from the rest of the parameter. This means that comparing the same tracks for a different observed luminosity needs to be done very carefully since the uncertainties of the luminosities are different, and the  $\chi^2$  are thereby automatically weighted differently.

More on if it is actually a problem.



## 9 Conclusions



# Bibliography

- Aerts, Conny, Jørgen Christensen-Dalsgaard, & Donald W Kurtz (2010). *Asteroseismology*. Springer Science & Business Media.
- Andrae, René et al. (2018). “Gaia Data Release 2-First stellar parameters from Apsis”. In: *Astronomy & Astrophysics* 616, A8.
- Antoci, V et al. (2011). “The excitation of solar-like oscillations in a  $\delta$  Sct star by efficient envelope convection”. In: *Nature* 477.7366, p. 570.
- Antoci, Victoria Laura (2011). “Solar-like oscillations in Delta Scuti stars”. PhD thesis. uniwien.
- Antoci, V et al. (2007). “Is 44 Tauri an exceptional case among the  $\delta$  Scuti stars?” In: *Astronomy & Astrophysics* 463.1, pp. 225–232.
- Antoci, V et al. (2014). “The role of turbulent pressure as a coherent pulsational driving mechanism: The case of the  $\delta$  Scuti star HD 187547”. In: *The Astrophysical Journal* 796.2, p. 118.
- Asplund, Martin et al. (2009). “The chemical composition of the Sun”. In: *Annual review of astronomy and astrophysics* 47, pp. 481–522.
- Balona, LA et al. (2011). “Kepler observations of Am stars”. In: *Monthly Notices of the Royal Astronomical Society* 414.1, pp. 792–800.
- Borucki, W, D Koch, N Batalha, et al. (2009). *Transiting Planets (IAU Symp. 253)*, ed.
- Breger, M. & P. Lenz (Sept. 2008). “Amplitude variability and multiple frequencies in 44 Tauri: 2000-2006”. In: *Astronomy & Astrophysics* 488, pp. 643–651. arXiv: 0807.3219.
- Brown, AGA et al. (2018). “Gaia Data Release 2-Summary of the contents and survey properties”. In: *Astronomy & astrophysics* 616, A1.
- Cassisi, Santi et al. (2007). “Updated electron-conduction opacities: the impact on low-mass stellar models”. In: *The Astrophysical Journal* 661.2, p. 1094.
- Christensen-Dalsgaard, J (1984). “What will asteroseismology teach us”. In: *Space Research in Stellar Activity and Variability*, p. 11.
- Christensen-Dalsgaard, Jørgen (2008a). “ADIPLS—the Aarhus adiabatic oscillation package”. In: *Astrophysics and Space Science* 316.1-4, pp. 113–120.
- (2008b). *Lecture notes on stellar structure and evolution*. Aarhus Universitet. Institute for Fysik og Astronomi.
- Cody, Ann Marie & Lynne A Hillenbrand (2014). “A pulsation search among young brown dwarfs and very-low-mass stars”. In: *The Astrophysical Journal* 796.2, p. 129.

- Dupret, M-A et al. (2004). "Theoretical instability strips for  $\delta$  Scuti and  $\gamma$  Doradus stars". In: *Astronomy & Astrophysics* 414.2, pp. L17–L20.
- Dupret, M-A et al. (2005). "Time-dependent convection seismic study of  $\delta$  Sct stars". In: *Monthly Notices of the Royal Astronomical Society* 361.2, pp. 476–486.
- Dziembowski, W & M Królikowska (1990). "On the mechanism of mode selection in Delta Scuti stars". In: *Acta Astronomica* 40, pp. 19–26.
- Eggleton, Peter P (1971). "The evolution of low mass stars". In: *Monthly Notices of the Royal Astronomical Society* 151.3, pp. 351–364.
- Ferguson, Jason W et al. (2005). "Low-temperature opacities". In: *The Astrophysical Journal* 623.1, p. 585.
- Flower, P. J. (Sept. 1996). "Transformations from Theoretical Hertzsprung-Russell Diagrams to Color-Magnitude Diagrams: Effective Temperatures, B-V Colors, and Bolometric Corrections". In: *The Astrophysical Journal* 469, p. 355.
- Freedman, Richard S, Mark S Marley, & Katharina Lodders (2008). "Line and mean opacities for ultracool dwarfs and extrasolar planets". In: *The Astrophysical Journal Supplement Series* 174.2, p. 504.
- Gehmeyr, M & D Mihalas (1994). "Adaptive grid radiation hydrodynamics with TITAN". In: *Physica D: Nonlinear Phenomena* 77.1-3, pp. 320–341.
- Gilliland, Ronald L et al. (2010). "Kepler asteroseismology program: introduction and first results". In: *Publications of the Astronomical Society of the Pacific* 122.888, p. 131.
- Grevesse, N & A Noels (1993). "Cosmic abundances of the elements." In: *Origin and Evolution of the Elements*, pp. 15–25.
- Grevesse, N & AJ Sauval (1998). "Standard solar composition". In: *Space Science Reviews* 85.1-2, pp. 161–174.
- Grigahcène, A et al. (2005). "Convection-pulsation coupling-I. A mixing-length perturbative theory". In: *Astronomy & Astrophysics* 434.3, pp. 1055–1062.
- Heiter, U et al. (2002). "New grids of ATLAS9 atmospheres I: Influence of convection treatments on model structure and on observable quantities". In: *Astronomy & Astrophysics* 392.2, pp. 619–636.
- Henyey, LG et al. (1959). "A Method for Automatic Computation of Stellar Evolution." In: *The Astrophysical Journal* 129, p. 628.
- Herwig, Falk (2004). "Evolution and yields of extremely metal-poor intermediate-mass stars". In: *The Astrophysical Journal Supplement Series* 155.2, p. 651.
- Houdek, G. et al. (Nov. 1999). "Amplitudes of stochastically excited oscillations in main-sequence stars". In: *Astronomy & Astrophysics* 351, pp. 582–596. eprint: [astro-ph/9909107](https://arxiv.org/abs/astro-ph/9909107).

- Iben Jr, Icko (1967). “Stellar evolution within and off the main sequence”. In: *Annual Review of Astronomy and Astrophysics* 5.1, pp. 571–626.
- Kippenhahn, Rudolf, Alfred Weigert, & Achim Weiss (1990). *Stellar structure and evolution*. Vol. 192. Springer.
- Koch, David G et al. (2010). “Kepler mission design, realized photometric performance, and early science”. In: *The Astrophysical Journal Letters* 713.2, p. L79.
- Lenz, P et al. (2008). “An asteroseismic study of the  $\delta$  Scuti star 44 Tauri”. In: *Astronomy & Astrophysics* 478.3, pp. 855–863.
- Lenz, P et al. (2010). “A  $\delta$  Scuti star in the post-MS contraction phase: 44 Tauri”. In: *Astronomy & Astrophysics* 509, A90.
- Lesaffre, Pierre et al. (2006). “The C flash and the ignition conditions of Type Ia supernovae”. In: *Monthly Notices of the Royal Astronomical Society* 368.1, pp. 187–195.
- Matthews, Jaymie M (2007). “One small satellite, so many light curves: Examples of delta Scuti asteroseismology from the MOST space mission<sup>1</sup>”. In: *Communications in Asteroseismology* 150, p. 333.
- McNamara, DH & JM Powell (1985). “RELATIONS BETWEEN (FE/H) AND DELTA-M 1 FOR F AND EARLY-G STARS.” In: *Publications of the Astronomical Society of the Pacific* 97.597, p. 1101.
- Michel, Eric et al. (2008). “First asteroseismic results from CoRoT”. In:
- Nendwich, Johannes et al. (2004). “Interpolation of Stellar Model Grids and Application to the NEMO Grid”. In: *arXiv preprint astro-ph/0406381*.
- Nordlund, Å & RF Stein (1990). “3-D simulations of solar and stellar convection and magnetoconvection”. In: *Computer Physics Communications* 59.1, pp. 119–125.
- Paczynski, B (1969). “Envelopes of red supergiants”. In: *Acta Astronomica* 19, p. 1.
- Palla, Francesco & Isabelle Baraffe (2005). “Pulsating young brown dwarfs”. In: *Astronomy & Astrophysics* 432.2, pp. L57–L60.
- Pamyatnykh, AA (2000). “Pulsational instability domain of Delta Scuti variables”. In: *arXiv preprint astro-ph/0005276*.
- Paxton, Bill (2004). “EZ to evolve ZAMS stars: A program derived from Eggleton’s Stellar Evolution Code”. In: *Publications of the Astronomical Society of the Pacific* 116.821, p. 699.
- Paxton, Bill et al. (2013). “Modules for experiments in stellar astrophysics (MESA): planets, oscillations, rotation, and massive stars”. In: *The Astrophysical Journal Supplement Series* 208.1, p. 4.

- Paxton, Bill et al. (2015). “Modules for experiments in stellar astrophysics (MESA): binaries, pulsations, and explosions”. In: *The Astrophysical Journal Supplement Series* 220.1, p. 15.
- Paxton, Bill et al. (2018). “Modules for Experiments in Stellar Astrophysics (): Convective Boundaries, Element Diffusion, and Massive Star Explosions”. In: *The Astrophysical Journal Supplement Series* 234.2, p. 34.
- Paxton, Bill et al. (2019). “Modules for Experiments in Stellar Astrophysics (MESA): Pulsating Variable Stars, Rotation, Convective Boundaries, and Energy Conservation”. In: *arXiv preprint arXiv:1903.01426*.
- Paxton, Bill et al. (2010). “Modules for experiments in stellar astrophysics (MESA)”. In: *The Astrophysical Journal Supplement Series* 192.1, p. 3.
- Pols, Omno R et al. (1995). “Approximate input physics for stellar modelling”. In: *Monthly Notices of the Royal Astronomical Society* 274.3, pp. 964–974.
- Potekhin, Alexander Y & Gilles Chabrier (2010). “Thermodynamic functions of dense plasmas: analytic approximations for astrophysical applications”. In: *Contributions to Plasma Physics* 50.1, pp. 82–87.
- Preston, George W (1974). “The chemically peculiar stars of the upper main sequence”. In: *Annual review of astronomy and astrophysics* 12.1, pp. 257–277.
- Rogers, FJ & A Nayfonov (2002). “Updated and expanded OPAL equation-of-state tables: implications for helioseismology”. In: *The Astrophysical Journal* 576.2, p. 1064.
- Royer, F, J Zorec, & AE Gómez (2004). “Rotational velocity distributions of A-type stars”. In: *Proceedings of the International Astronomical Union* 2004.IAUS224, pp. 109–114.
- Samadi, R., M.-J. Goupil, & G. Houdek (Nov. 2002). “Solar-like oscillations in delta Scuti stars”. In: *Astronomy & Astrophysics* 395, pp. 563–571. eprint: [astro-ph/0208573](#).
- Saumon, D, G Chabrier, & HM Van Horn (1995). “An equation of state for low-mass stars and giant planets”. In: *The Astrophysical Journal Supplement Series* 99, p. 713.
- Smalley, B et al. (2011). “SuperWASP observations of pulsating Am stars”. In: *Astronomy & Astrophysics* 535, A3.
- Solano, E & J Fernley (1997). “Spectroscopic survey of δ Scuti stars-I. Rotation velocities and effective temperatures”. In: *Astronomy and Astrophysics Supplement Series* 122.1, pp. 131–147.
- Starrfield, Sumner et al. (2000). “The effects of new nuclear reaction rates and opacities on hydrodynamic simulations of the nova outburst”. In: *The Astrophysical Journal Supplement Series* 127.2, p. 485.

- Tassoul, Monique (1980). “Asymptotic approximations for stellar nonradial pulsations”. In: *The Astrophysical Journal Supplement Series* 43, pp. 469–490.
- (1990). “Second-order asymptotic approximations for stellar nonradial acoustic modes”. In: *The Astrophysical Journal* 358, pp. 313–327.
- Timmes, Frank X & F Douglas Swesty (2000). “The accuracy, consistency, and speed of an electron-positron equation of state based on table interpolation of the Helmholtz free energy”. In: *The Astrophysical Journal Supplement Series* 126.2, p. 501.
- Townsend, RHD, J Goldstein, & EG Zweibel (2017). “Angular momentum transport by heat-driven g-modes in slowly pulsating B stars”. In: *Monthly Notices of the Royal Astronomical Society* 475.1, pp. 879–893.
- Townsend, RHD & SA Teitler (2013). “GYRE: an open-source stellar oscillation code based on a new Magnus Multiple Shooting scheme”. In: *Monthly Notices of the Royal Astronomical Society* 435.4, pp. 3406–3418.
- Townsend, Richard (2013). *Gyre*. <https://bitbucket.org/rhdtownsend/gyre/wiki/Home>. [Online; accessed 13-November-2018].
- Trampedach, Regner & Robert F Stein (2011). “The mass mixing length in convective stellar envelopes”. In: *The Astrophysical Journal* 731.2, p. 78.
- Turcotte, S. et al. (Aug. 2000). “The effect of diffusion on pulsations of stars on the upper main sequence —  $\delta$  Scuti and metallic A stars”. In: *Astronomy & Astrophysics* 360, pp. 603–616. eprint: astro-ph/0006272.
- Walker, Gordon et al. (2003). “The MOST asteroseismology mission: Ultraprecise photometry from space”. In: *Publications of the Astronomical Society of the Pacific* 115.811, p. 1023.
- Wanner, Gerhard & Ernst Hairer (1996). *Solving ordinary differential equations II*. Springer Berlin Heidelberg.
- Weiss, Achim & Helmut Schlattl (2008). “GARSTEC—the Garching Stellar Evolution Code”. In: *Astrophysics and Space Science* 316.1-4, pp. 99–106.
- Weiss, Achim et al. (2004). “Cox and Giuli’s Principles of Stellar Structure”. In: *Cox and Giuli’s Principles of Stellar Structure, by A. Weiss, W. Hillebrandt, HC. Thomas, H. Ritter. Cambridge, UK: Cambridge Scientific Publishers Ltd, 2004*.
- Young, Patrick A & David Arnett (2005). “Observational tests and predictive stellar evolution. II. Nonstandard models”. In: *The Astrophysical Journal* 618.2, p. 908.
- Zima, Wolfgang et al. (2007). “High-resolution spectroscopy of the  $\delta$  Scuti star 44 Tauri: photospheric element abundances and mode identification”. In: *Astronomy & Astrophysics* 471.1, pp. 237–245.